International Journal of Geosciences, 2023, 14, 999-1035
https://www.scirp.org/journal/ijg
ISSN Online: 2156-8367
ISSN Print: 2156-8359

Comprehensive Review of Studies on Metamorphic Rocks

Hakan Citak[1], Mustafa Coramik[2], Huseyin Gunes[3], Sabri Bicakci[4], Yavuz Ege[2*]

[1]Department of Electric and Energy, Balikesir Vocational High School, Balikesir University, Balikesir, Turkey
[2]Department of Physics, Necatibey Faculty of Education, Balikesir University, Balikesir, Turkey
[3]Department of Computer Engineering, Faculty of Engineering, Balikesir University, Balikesir, Turkey
[4]Department of Electric and Electronics Engineering, Faculty of Engineering, Balikesir University, Balikesir, Turkey
Email: hcitak@balikesir.edu.tr, mustafacoramik@balikesir.edu.tr, hgunes@balikesir.edu.tr, sbicakci@balikesir.edu.tr, *yege@balikesir.edu.tr

How to cite this paper: Citak, H., Coramik, M., Gunes, H., Bicakci, S. and Ege, Y. (2023) Comprehensive Review of Studies on Metamorphic Rocks. *International Journal of Geosciences*, **14**, 999-1035.
https://doi.org/10.4236/ijg.2023.1410052

Received: September 8, 2023
Accepted: October 28, 2023
Published: October 31, 2023

Abstract

Marble is a metamorphic rock, which is one of the 3 basic rock types (magmatic, sedimentary, metamorphic) forming the earth's crust. The major characteristic sought after in a rock mass in the field for it to be exportable and usable as marble is its suitability to be cut in blocks. In the process of producing marble slabs from marble blocks, the blocks are expected not to contain potentially problematic hard or weak zones and their geomechanical and chemical properties should conform to the relevant standards. Ignoring of the geological properties of the rock in the process of deciding for marble production at a marble site and determination of production location, direction and method is the most important parameter that would increase production loss. In order to reduce losses by determination of geological properties of marble, many academic studies have been conducted on the effects of water saturation, temperature, freezing and thawing on its mechanical and fracture properties. There are further studies on crack propagation in marble under stress. However, even those marble blocks that are obtained based on geological parameters may suffer serious cracks or fractures due to stresses caused by their weight and geometry. Therefore, cutting direction is of critical importance in order to minimize marble waste in the process of cutting a marble block which is brought to the inventory or processing site with cracks, cavities or fractures. Certain studies exist within such context, where the geometry of the discontinuity within a block is determined using non-destructive methods, such as ultrasonic testing, in order to determine the appropriate cutting direction. Such studies made use of ultrasonic waves to determine the physical and chemical structures of magmatic and sedimentary rocks by measuring the progress velocity of sonic waves in the rock. Said studies,

however, mostly worked on sedimentary and magmatic rock specimens, focusing less on metamorphic rocks such as marble due to their anisotropic properties. Understanding the academic literature studies on marble would provide significant contribution to the reduction of production losses during the processing marble blocks in processing plants and the achievement of production efficiency levels that are within economic limits. Within such scope, this study has reviewed the past academic studies on marble, classified them under 6 categories, and comprehensively analyzed each category based on materials, testing setups, test specimens, test parameters and research techniques.

Keywords

Marble, Metamorphic Rock, Ultrasonic Test, Crack, Cutting Direction

1. Introduction

The term marble represents metamorphic rocks with crystalline inner structure, which were formed through metamorphosis of sedimentary rocks containing high levels of calcium carbonate (95% $CaCO_3$), lower levels of magnesium carbonate ($MgCO_3$) and various metal oxides (quartz, graphite, hematite, limonite, pyrite, mica, chlorite, etc.) due to exposure to pressure and heat within extended geological periods. Low metal oxide content gives marble a variety of colors and a grainy appearance. In addition, increasing SiO_2 content makes the rock harder, while increasing MgO content makes it more brittle and increasing Fe_2O_3 content makes it darker in color [1]. Block efficiency is also quite important for marble, in addition to its color, pattern, texture and cuttability. On the other hand, a marble block is required not to contain any weak zones that could create problems in slab production, to be able to receive a uniform amount of finish on the entire slab surface, to have physical, geomechanical and chemical properties which conform to the relevant standards, and to be resistant to atmospheric and chemical effects. Determination of the optimal cutting direction is required in order to minimize marble waste in the process of cutting a marble block which is brought to the inventory site [2]. This, on the other hand, would only be possible by determining the physico-mechanical properties of marble (mineral orientation, fractures and cracks, porosity, permeability, anisotropy, surface hardness, density, resistance to freezing, pressure and abrasion resistance, compression strength and Young's modulus, Poisson's ratio, modulus of elasticity, etc.), as well as the geometry of the discontinuity, if any, inside the marble block. Accordingly, academic studies have been conducted for various types of marble, on the effects of water saturation, temperature, freezing and thawing on its mechanical and fracture properties. The literature also includes studies on crack propagation in marble under stress, as well as determination of discontinuities in a marble block using non-destructive testing methods (Ultrasonic, GPR, etc.) [3]. Dy-

namic physical properties (Lame Coefficients, Poisson's Ratio, Young's Modulus, Bulk Modulus, Coefficient of Compressibility, Dynamic Elastic Constants, Compression strength, etc.) and chemical structure of marble were determined based on the change of progress velocity of ultrasonic waves (Compressional P, Shear S) in marble [4] [5].

This study reviews and classifies past studies on marble in 6 main categories with the aim of contributing to ability to keep the production efficiency of marble, a metamorphic rock, within the economic limit values. Said categories are, 1) studies on crack propagation in marble under stress and mechanical and fracture properties of marble, 2) effects of freezing and thawing on the mechanical properties of marble, 3) effects of water saturation on mechanical properties and fracture behavior of marble, 4) effects of temperature on the micro-structure and physico-mechanical properties of marble, 5) determination of discontinuities in marble sites, and 6) crack assessment in marble sculptures. The study addresses each category individually, presenting and analyzing them in detail based on materials, testing setups, test specimens, test parameters and research techniques. To ensure better understanding of the categories, the paper first explains the application principles of the research techniques used in marble-related studies. The aim of this study was to determine the developments in the production processes of marble by compiling the previous literature, thus contributing to reducing marble waste and increasing production efficiency.

2. Techniques Used in Marble-Related Research Studies

2.1. Acoustic Emission (AE) Method

Acoustic emissions (AE) are high-frequency (20 kHz - 1 MHz) stress waves created as a result of crack formation and fracture propagation behavior of a material/structure due to quick release of temporary energy from limited resources. AE testing involves recording of such waves using piezoelectric sensors located on the surface of the tested structure and subsequent analysis of the recorded signals to gain an understanding of the nature of their sources. Various parameters exist in relation with acoustic emission signals, including peak amplitude, RMS, counts, cumulative counts, rise time and event time (**Figure 1**). Such parameters provide vital information for the determination of mechanical and fracture properties of marble. However, background noise should be filtered in order to accurately determine the parameters. Acoustic emission test noise comprises of undesired signals such as 1) mechanical noise, 2) hydraulic noise, 3) electrical (electro-magnetic) noise that are sensed by the transformer. Mechanical and hydraulic noise originates from the uniaxial compression device, while electromagnetic interference (EMI) originates from the AE instrumentation because of electrical transmission and radiation. Electromagnetic noise can be prevented by providing better protection of sensors, preamplifier and main amplifier in metal casings with high conductivity, as well as by earthing casings at a common point. Isolating the transformer in the power source may also reduce EMI.

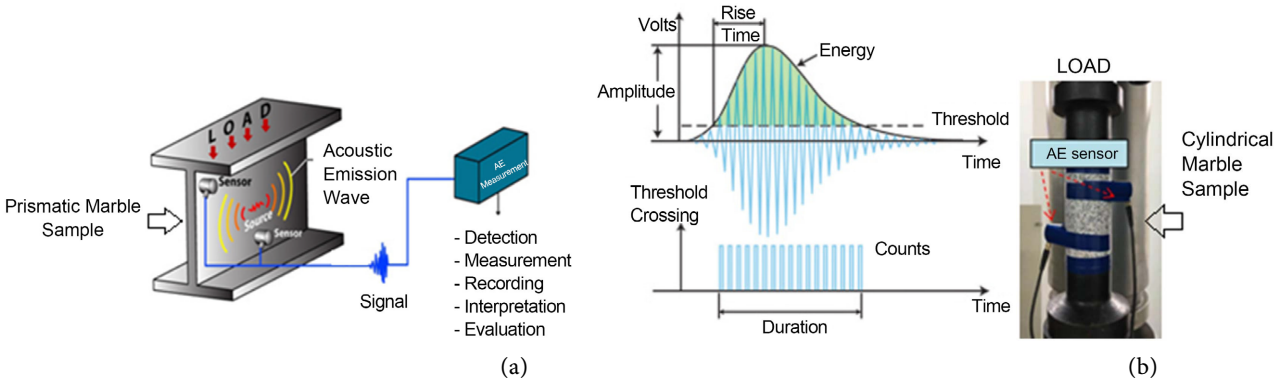

Figure 1. (a) Acoustic emission method and its output, (b) contact of acoustic sensors with marble for cylindrical marble [6].

The low-amplitude, high-frequency acoustic emission wave generated in the marble under load are transformed into electric signals by piezoelectric sensors, after which they are subjected to a series of electronic processes. Subsequent to the data processing phase, which involves amplification, filtering, data collection via an 18 bit, 40 MS/s A/D converter module and DSP-based FPGA, the signal is transmitted to a PC and displayed. Electronic structure of an AE measurement device which runs such processes is exhibited in **Figure 2**.

2.2. Real-Time Ultrasonic Detection Method

Ultrasonic test is performed using receiving and transmitting piezoelectric sensors. Ultrasonic waves (P and S) applied to the test subject by the transmitting sensor are received by the receiving sensor, and the time spent by the wave inside the specimen is measured by the ultrasonic test device. The test device needs to be prepared for measurement beforehand. Such preparation includes entering marble density, pulse voltage, wave type and gain value into the device. Subsequently, the sensors should be placed on top of each other and calibrated. Then, silicone grease should be applied as adhesive on both surfaces of the marble block and on the sensors. Following the time information, which is often determined by direct contact, the device performs the calculations by respectively running the theoretical equations provided in **Table 1**. Compressional wave velocity is measured first, using data for specimen thickness and the determined time. Then, shear wave velocity is calculated by dividing the compressional wave velocity by two. The μ and σ Lame coefficients are calculated using the density data initially entered into the device and the two aforementioned velocity values. Lastly, the calculated Lame coefficients are used to calculate the Poisson's ratio, Young's modulus, bulk modulus, coefficient of compressibility and dynamic elastic constants, respectively.

Mineralogy of the tested material, the shape and dimensions of the spaces-grains and their micro-structural properties, such as distribution, determines the progress of the ultrasonic velocity. Said material properties uniquely alter the frequency spectrum and defines the compressional and shear wave velocities of various types of progress. Therefore, wave velocities and amplitude-frequency

spectrums are closely related to the physical and mechanical properties of the material (Poisson's ratio, Young's modulus, bulk modulus, efficient of compressibility and dynamic elastic constants), which are in turn closely related to its micro-structural properties.

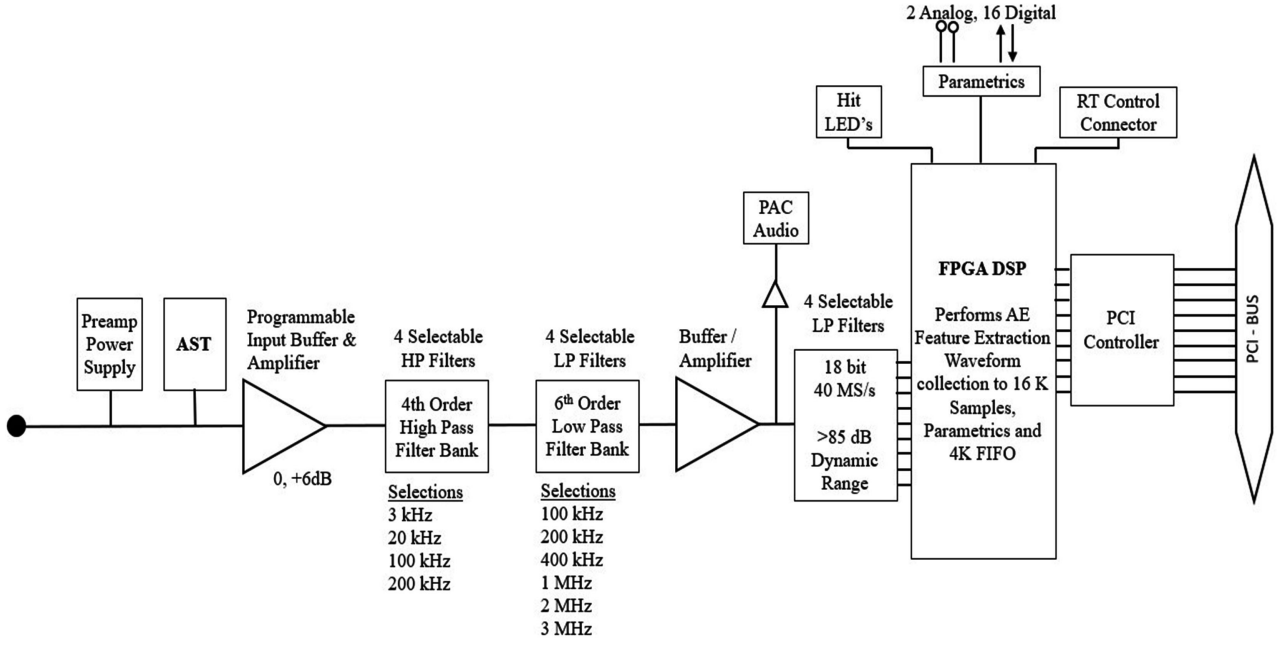

Figure 2. Electronics of acoustic emission measuring device [7].

Table 1. Theoretical equations of test parameters [8].

Parameter	Equations	Definitions
v_s and v_p wave velocity	$v = \frac{x}{t}$ (m/s)	x: Marble thickness t: Duration of passage
μ Lame constant	$v_s = \sqrt{\frac{\mu}{\rho}}$ (m/s)	v_s: Transverse wave velocity ρ: Marble density
λ Lame constant	$v_p = \sqrt{\frac{\lambda + 2\mu}{\rho}}$ (m/s)	v_p: Longitudinal wave velocity
σ Poisson ratio	$\sigma = \frac{\lambda}{2 \times (\lambda + \mu)}$	
Y Young modulus	$Y = \frac{\mu \times (3\lambda + 2\mu)}{\lambda + \mu}$ (N/m^2)	
B Volume modulus	$B = \lambda + 2\mu$ (N/m^2)	
K Compression coefficient	$K = \frac{1}{B}$ (m^2/N)	
E Dynamic Elastic Constant	$E = \frac{(1+\sigma) \times (1-2\sigma)}{(1-\sigma)} \times v_p^2 \times \frac{\rho}{g} \times 10^5$ (kg/cm^2)	

Ultrasonic test is carried out both under load and without load, the latter being carried out particularly in determining discontinuities in a specimen. Further, the surface needs to be polished in order to achieve good ultrasonic transmission. Acoustic emission similarly involves ultrasonic wave detection. However, in that case, the sound source is the material itself and the signal created by such sound in the sensor is analyzed. On the other hand, ultrasonic test involves simultaneous assessment of the receiving and transmitting signals. Figure 3 exhibits the application of the ultrasonic test on cylindrical and prismatic specimens, and Figure 4 demonstrates a comparison of ultrasonic test outputs via AE.

(a)

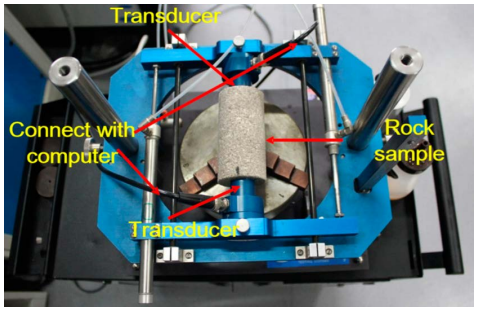

(b)

Figure 3. Application of ultrasonic testing to (a) prismatic, (b) cylindrical samples [8].

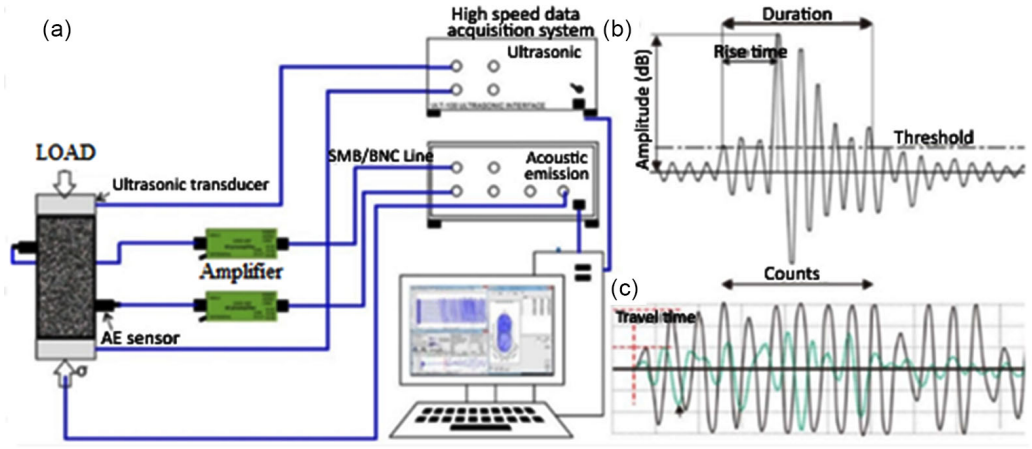

Figure 4. Diagram of the principle of ultrasonic detection and AE tracking during sample deformation. (a) connection of the AE device to the sample; (b) determining AE parameters from the waveform; (c) ultrasonic waveform to obtain the travel time [9].

2.3. Linear Variable Differential Transformers (LVDT)

LVDTs are a widely used type of transformers which can transform linear movements of an object, to which it is mechanically connected, into electric signals. These are able to measure small movements of various magnitudes, ranging from several millionths of an inch to several inches. Components of an LVDT able to detect positions up to ±30 inches (±0.762 meters) are shown in Figure 5. Internals of a transformer comprise of primary winding with a pair of identically wound secondary windings which are positioned symmetrically on both sides of the primary winding. The coils are wound on a monobloc hollow form of thermally stable glass-reinforced polymer, which is encapsulated against humidity, covered by a highly conductive magnetic shield and fixed on a cylindrical stainless-steel casing. This coil setup is usually the fixed component of the position sensor.

The moving component of an LVDT is a separate pipe-shaped armature made of magnetically conductive material. Being referred to as the core, this component can freely move axially inside the empty bore of the coil and is physically connected to the object the position of which is to be measured. Typically, the bore is large enough to provide a significant radial distance between the core and the bore, and there is no physical contact between the coils. In operation, the primary winding of the LVDT is energized with alternating current with appropriate amplitude and frequency, which is referred to as primary excitation. The electric output signal of the LVDT is the differential AC voltage between the two secondary windings, which varies based on the axial position of the core inside the LVDT coil. Said AC output voltage is often transformed into a higher-level DC voltage or current, which is more suitable for use in the relevant electronic circuits.

The primary winding of the LVDT, P, is energized by a constant-amplitude AC source. The magnetic flux thereby created is connected by the core to the adjacent secondary windings, S1 and S2. If the core is located halfway between S1 and S2, then it is connected to both secondaries with equal flux, in which case the voltages induced in the S1 and S2 windings are equal to E1 and E2, respectively. Differential voltage output (E1-E2) is essentially zero at this reference middle position of the core, which is therefore referred to as point zero. As shown in Figure 6; if the core is moved to a position which is closer to S1 than S2, then more flux would connect to S1 than to S2, which would cause an increase in the induced voltage E1 and a decrease in E2, which, in turn, would create a differential voltage (E1-E2). In contrast, if the core is moved closer S2, then more flux would connect to S2 than to S1, which would cause a decrease in E1 and an increase in E2, which, in turn, would also create a differential voltage (E2-E1).

2.4. Atomic Force Microscope (AFM)

An atomic force microscope (AFM) scans the surface of a specimen using a con-

sole with a very sharp tip. As the tip approaches the surface, the close-distance attractive force between the surface and the tip causes the console to deviate towards the surface. On the other hand, when the console gets closer to the surface in a manner that would cause the tip to contact it, a progressively increasing repulsive force comes into play, causing the console to deviate away from the surface.

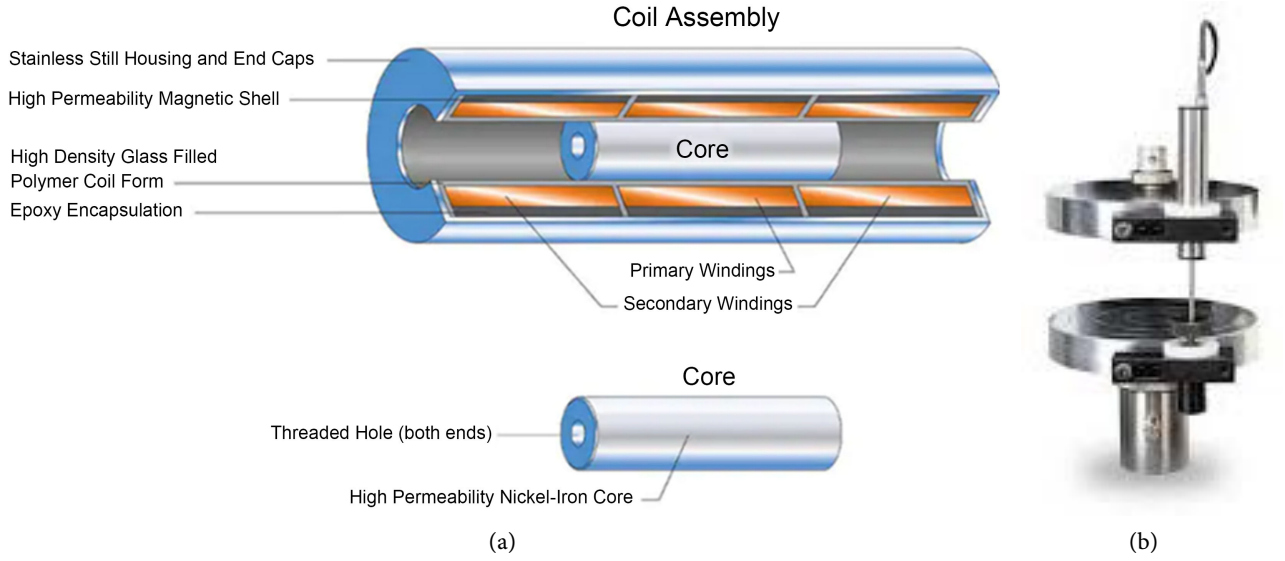

Figure 5. (a) Components of the LVDT, (b) its connection with the load handler [10].

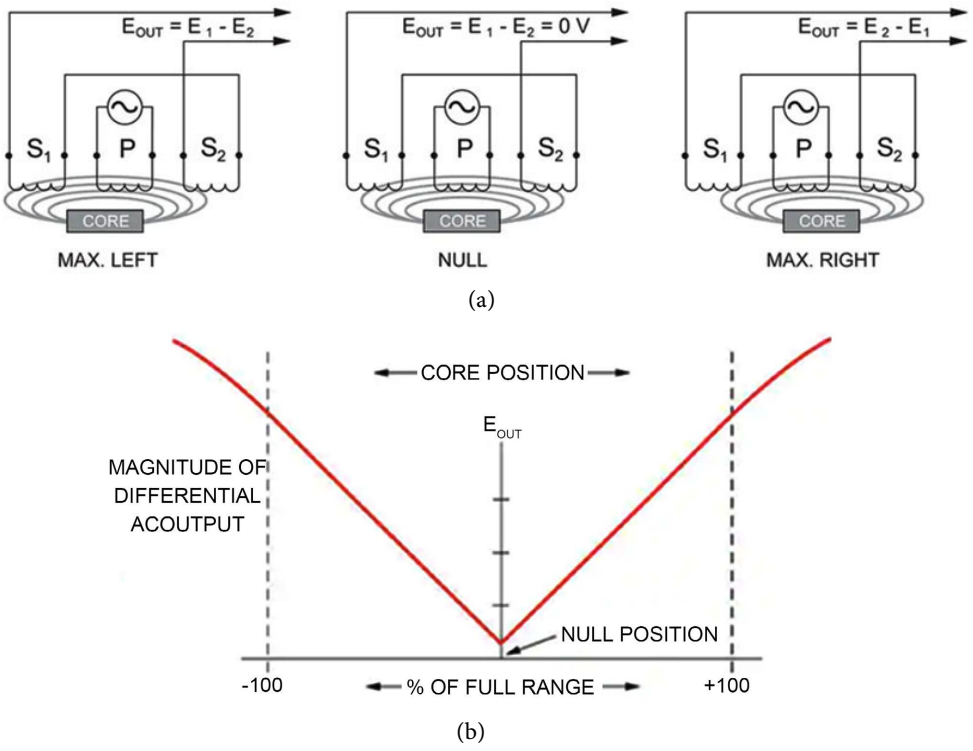

Figure 6. (a) Formation of the output voltage according to the position of the core in the LVDT, (b) its change [11].

A beam of laser is used to detect the deviations of the console towards or away from the surface. Any deviation of the console would cause small variations in the direction of the beam which is reflected from the flat top of the console. A position-sensitive photodiode (PSPD) can be used to track such variations. Thus, if an AFM tip passes over an elevated surface attribute, then the resulting console deviation (and the subsequent change in the direction of the reflected beam) is recorded by the PSPD.

The console of an AFM scans over the region of interest and displays its topography. Elevated and dented attributes on the specimen surface effects the console deviation which is monitored by the PSPD. Utilizing a feedback loop to control the height of the tip above the surface, thereby preserving a constant laser position, AFMs are capable of creating an accurate topographical map of surface attributes (**Figure 7**).

Surface scan by an AFM is achieved not by the movement of the console but by the movement, in the x, y, z directions, of the specimen placed on a piezoelectric material. Piezoelectric materials (piezo crystals) are ceramic materials that could enlarge or contract when voltage is applied. This allows the specimen to make very precise movements in the x, y, z directions (the position can be controlled in resolutions in nanometer levels).

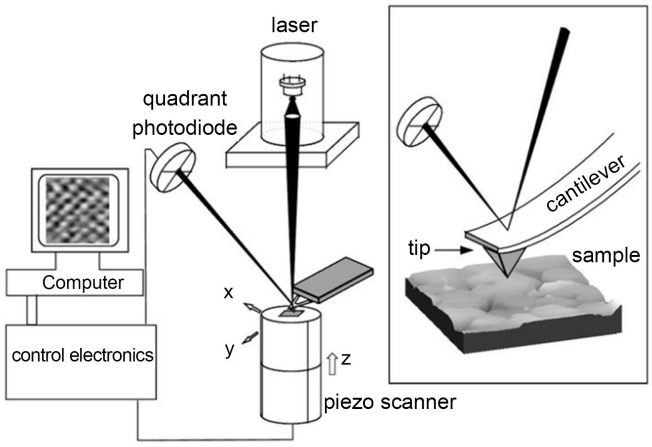

(a)

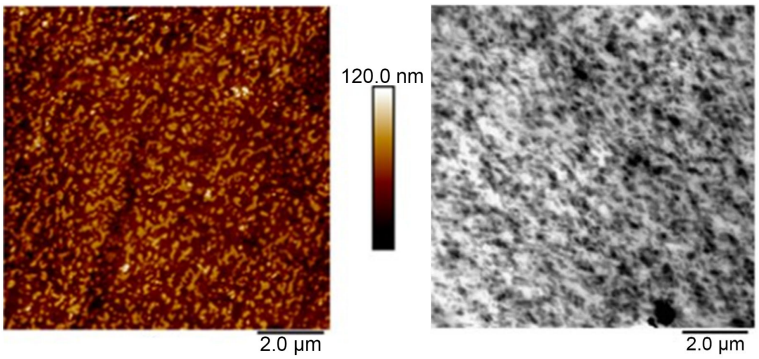

(b) (c)

Figure 7. (a) An AFM setup, (b) AFM image, (c) TEM image [12].

2.5. Environmental Scanning Electron Microscope (ESEM), SEM and TEM

Environmental scanning electron microscope (ESEM) is a direct descendant of the conventional SEM, but also allows scanning of wet and non-conducting specimens without any prior specimen preparation. A low gas pressure (up to approximately 10 torr) can be applied around the specimen. When water is used instead of gas, hydrated specimens can be kept in their natural state. Be it water or any other gas, ions created as a result of the collisions of the electrons emitted from the specimen and the gas molecules help reducing the creation of charges and are dragged back to the specimen surface. This eliminates the need to apply conductive surface coating to non-conductive specimens (**Figure 8(a)**). Such two significant benefits of ESEM makes the strengths of the scanning electron microscope (SEM) available for a wide range of materials. Additionally, a comparison of the operating conditions of ESEM and SEM is given in **Table 2**.

In conventional scanning electron microscope (SEM) systems, the surface of a solid specimen is excited by a highly focused energetic electron beam, which induces X-ray fluorescent from the elements comprising the specimen. Specimens need to be operated under high vacuum conditions and need to be conductive or coated with a conductive material, such as gold, in order to ensure proper analysis. In conventional SEMs, X-ray micro-analysis is prevented for non-coated non-conductive specimens due to specimen loading which could reduce the energy of the electron beam and renders quantitative analysis impossible. Environmental Scanning Electron Microscope (ESEM) is a unique system which allows analysis of non-coated biological and industrial materials, such as marble, by an electron beam in a water vapor atmosphere at high room pressure. Thus, specimens can be analyzed using ESEM without the need for destruction or any additional preparation procedures. The main drawback of a typical ESEM, however, is that the electron beam propagates in the high-pressure environment chamber and excites fluorescent X-rays not only under the beam but from the entire specimen. Fluorescent X-rays emitted from outside the area of interest are

Table 2. Comparison of operating conditions of ESEM and SEM.

Operating Conditions	Conventional SEM	Environmental SEM
Imaging Modes	Secondary Electrons (ET) Backscattered Electrons	Secondary Electrons (ESD) Backscattered Electrons
Working Distance	6 - 40 mm	6 - 15 mm
Accelerating Voltage	1 - 30 kV, normally 20 kV	1 - 30 kV, normally 20 kV
Vacuum Conditions	10^{-5} to 10^{-3} Pa High vacuum	10^{-4} to 0.9 kPa. Normally 10 - 250 Pa.
Magnification	10 to 100.000 times	70 to 100.000 times
Resolution	1.8 to 60 nm, usually 4.5 nm	5 or 7 nm
Sample Requirement	Dry and conductive samples only.	Any samples type
Sample Exchange Time	3 - 5 minutes	30 - 60 seconds
Approximate Cost	$65.000 - 250.000	$179.000 - 250.000

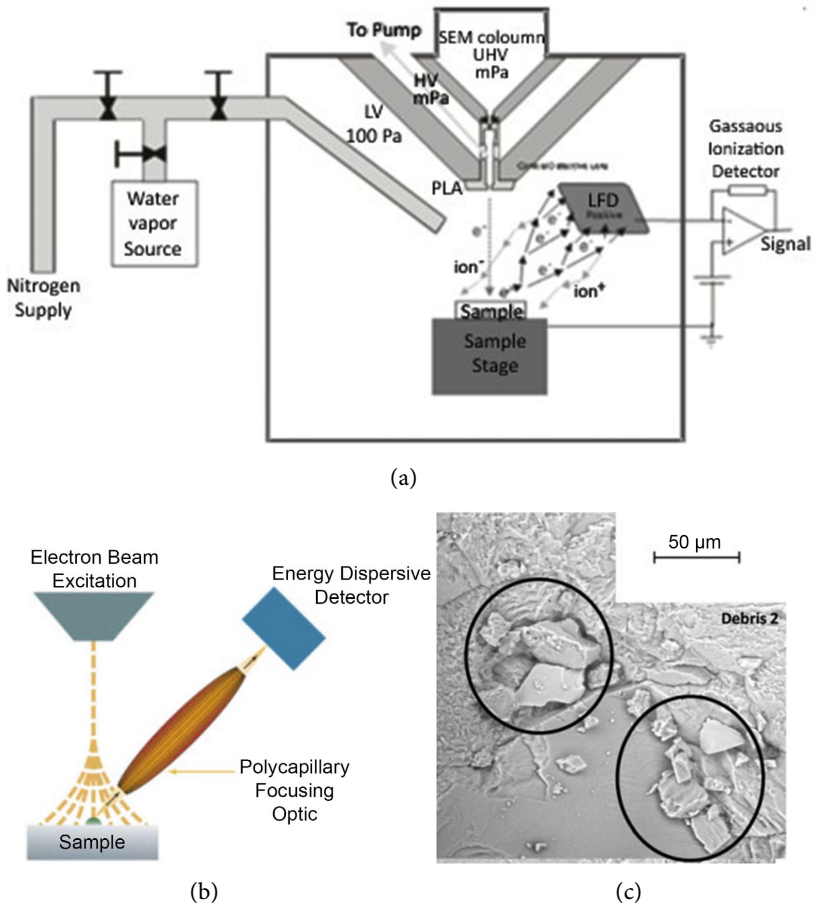

Figure 8. (a) Environmental scanning electron microscope (ESEM), (b) polycapillary addition to ESEM, (c) ESEM image of marble after mechanical cleaning [13].

also sensed by the detector and reduces image contrast. Polycapillary optics can be included into an existing ESEM in order to collect X-rays from an area defined by the focal point dimension and focus the same onto the detector, thereby reducing background noise and improve image contrast (**Figure 8(b)**, **Figure 8(c)**).

Both other electron microscope types (SEM and TEM) are equipped with energy-dissipating X-ray spectrometers. They are a strong tool to analyze chemical composition of a specimen. Each element emits an X-ray at a certain wavelength, its "fingerprint", which is detectable and analyzable. This allows matching of the elements on the sample area at an atomic resolution. SEM releases electrons, which scatter upon impact, and the specimen surface is thereby scanned. The device gathers the scattered electrons and creates an image. The image is displayed on a TV-like screen (**Figure 9(a)**, **Figure 9(b)**). On the other hand, TEM processes the specimen by sending an electron beam. The result is displayed using a fluorescent screen. SEM images are three-dimensional accurate representations, while TEM images are two-dimensional and require some interpretation (**Figure 9(c)**, **Figure 9(d)**). However, TEM has an advantage over SEM in terms of resolution and zooming (**Table 3**).

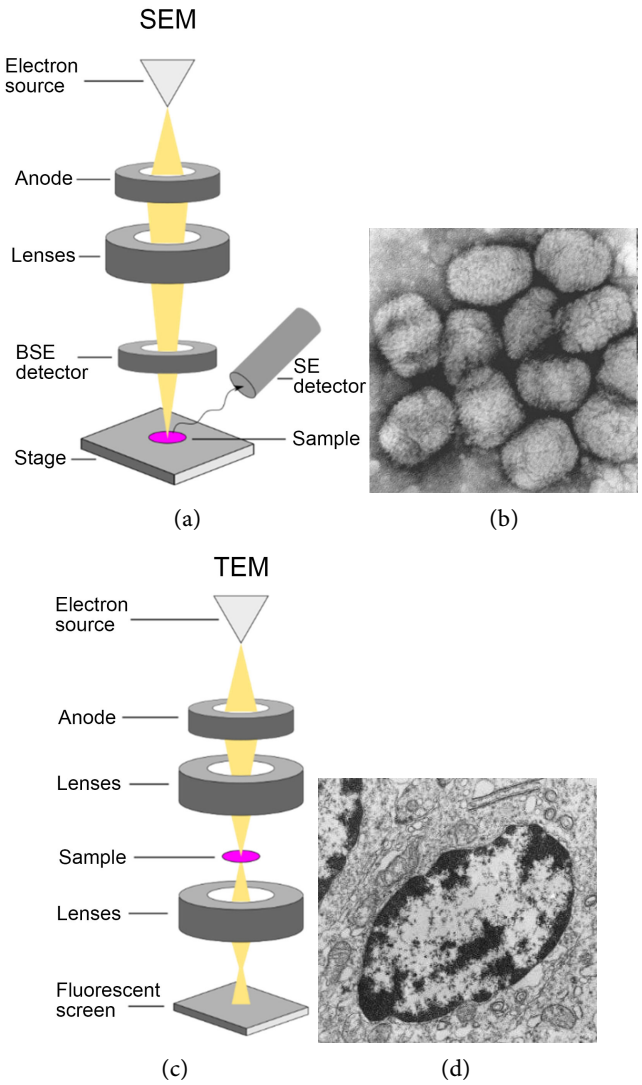

Figure 9. (a) Scanning electron microscope (SEM), (b) SEM image, (c) transmission electron microscope (TEM), (d) TEM image [14].

Table 3. Comparison of operating conditions of SEM and TEM.

	Scanning Electron Microscopes (SEM)	Transmission Electron Microscopes (TEM)
Electron stream	Fine, focused beam	Broad beam
Image taken	Topographical/surface	Internal structure
Resolution	Lower resolution	Higher resolution
Magnification	Up to 2,000,000 times	Up to 50,000,000 times
Image dimension	3-D	2-D
Sample thickness	Thin and thick samples okay	Ultrathin samples only
Penetrates sample	No	Yes
Sample restriction	Less restrictive	More restrictive
Sample preparation	Less preparation required	More preparation required
Cost	Less expensive	More expensive
Speed	Faster	Slower
Operation	Easy to use	More complicated; requires training

2.6. Micro-Computed Tomography (Micro-CT)

Micro-CT is a 3D imaging technique utilizing X-rays to see inside an object, slice by slice. In a Micro-CT system, X-rays are generated in an X-ray source, transmitted through the specimen, and recorded by the X-ray detector as a 2D projection image. The specimen is then rotated, and another X-ray projection image is taken (**Figure 10**). This step is repeated through a 180-degree turn (or sometimes 360 degrees, depending on specimen type). The series of X-ray projection images is then computed into cross-sectional images through the computational process called "reconstruction". These slices can be analyzed, further processed into 3D models, made into movies, printed into 3D physical objects, and more.

2.7. Discrete Element Method (DEM)

DEM (discrete element method) is a numerical technique for modeling the interaction between individual particles and boundaries in order to predict the behavior of cast solids. This device can easily model moving boundaries and used to better understand particle flow dynamics. The DEM method uses contact detection algorithms and can calculate the forces acting on particles by applying relevant contact models. Acceleration, velocity and position are then calculated using Newton's laws of motion and digital integration. The industry-leading software implementing the discrete element method (DEM) used to simulate the movement of granular and discontinuous material is ANSYS Rocky (**Figure 11**).

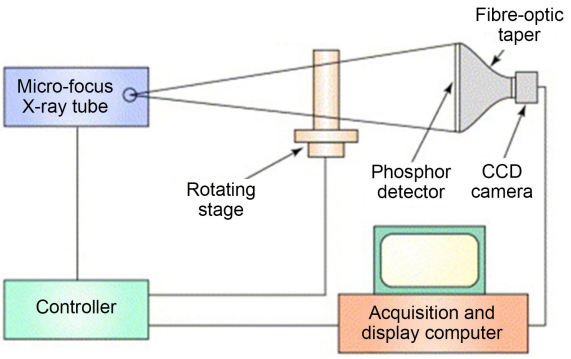

(a)

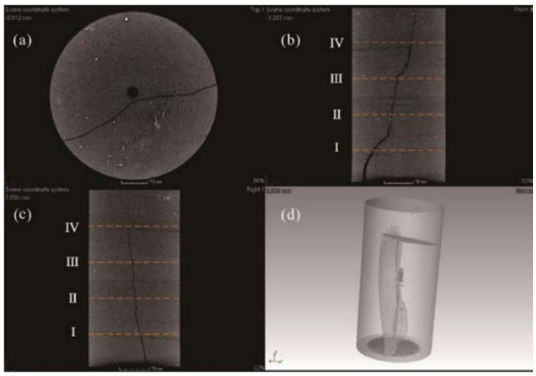

(b)

Figure 10. (a) Micro-CT System, (b) Micro-CT scan results for a marble sample [15].

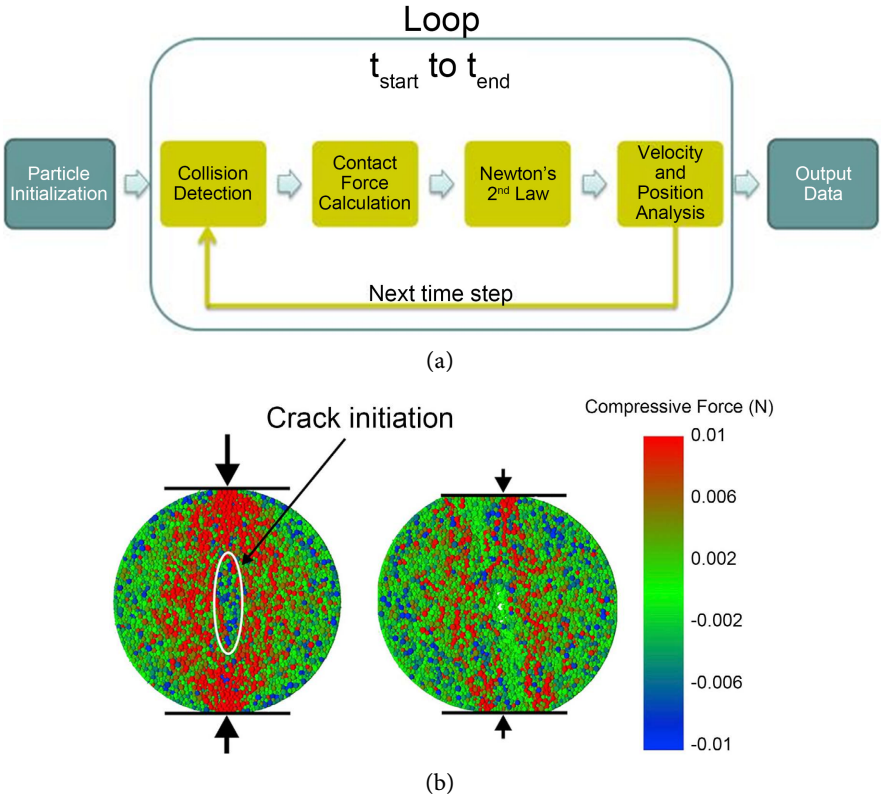

Figure 11. (a) DEM software cycle, (b) A DEM output [16].

2.8. Nuclear Magnetic Resonance (NMR)

In the Proton Nuclear Magnetic Resonance (Proton NMR) method, a specimen is placed in a strong magnetic field and subsequently subjected to impact by radio frequency radiation (**Figure 12**). The protons will have their spin states aligned or not aligned with the magnetic field, and the difference between such two states will create a resonance energy. When hit with the right frequency, protons with lower energy will reverse their alignment. As a result, what is detected using this technique is the energy emitted by those protons which revert back to the lower energy state (**Figure 13**).

2.9. Laser Ultrasonics Technique

Laser Ultrasonics is a contact-free ultrasonic analysis technique based on excitation and ultrasonic measurement using two lasers. A laser pulse is sent to the test specimen, creating an ultrasonic pulse which propagates throughout the material following interaction with the surface. The ultrasonic vibrations are measured using a laser vibrometer and displayed using a digital oscilloscope (**Figure 14**).

2.10. Polarized Light Microscopy

Polarized light microscopy is a contrast-enhancing technique which can be used to analyze the structure of an object (**Figure 15**). Polarized light microscopes have higher sensitivity and can be used in quantitative and qualitative research

studies. Polarized light microscopy is often used to analyze the anisotropy of a specimen's optical properties caused by stretching and deformation of initially isotropic materials. The specimens may be crystalline materials (pigments, minerals, etc.) and fibers as well as environmental particulate and biological materials. Polarized light microscopes are conventional standard microscopes equipped with two additional polarizing elements (polarizer and analyzer) which allow the specimen to be analyzed under polarized light. Polarized light microscopes allow observation of specimens that are visible primarily due to their optically anisotropic characteristics. Anisotropic materials have optical properties that vary with the crystallographic axis and direction of the incident light. Such materials have multiple refractive indices (e.g., azurite, cinnabar, etc.). However, these are polarization colors (not true specimen colors) and are related to the specimen's refractive indices and thickness. Isotropic materials (e.g., gases, liquids, resins, unstretched glasses, cubic crystals with only one refractive index) cannot be seen under cross-polarized light.

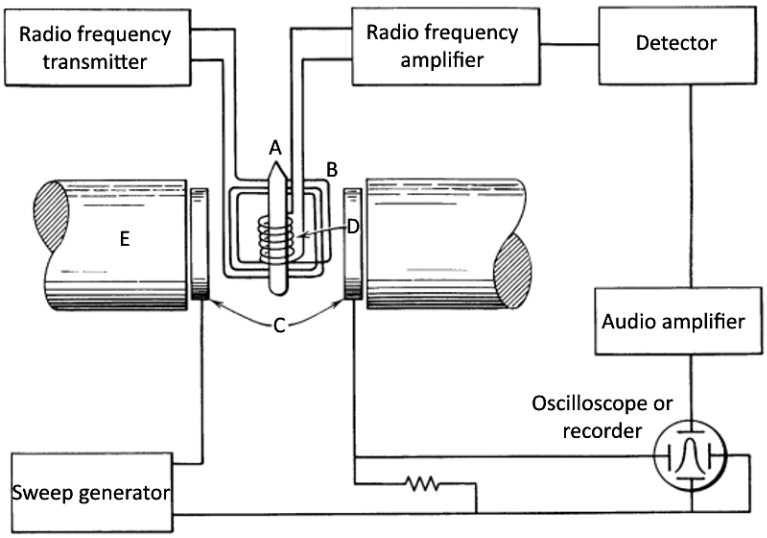

Figure 12. NMR System.

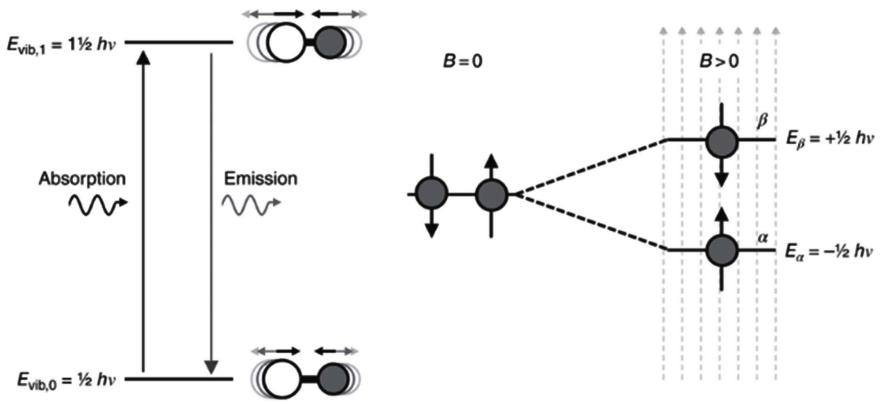

Figure 13. RF energy emission from the sample in the NMR system [17].

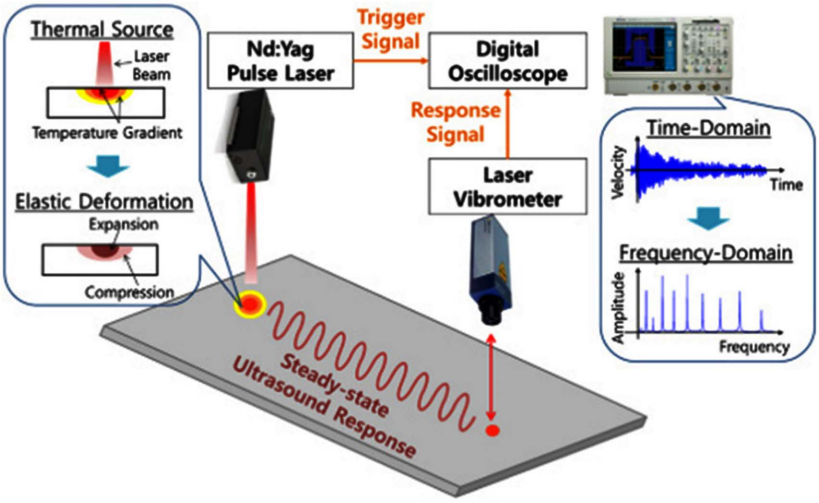

Figure 14. Laser ultrasonic technique [18].

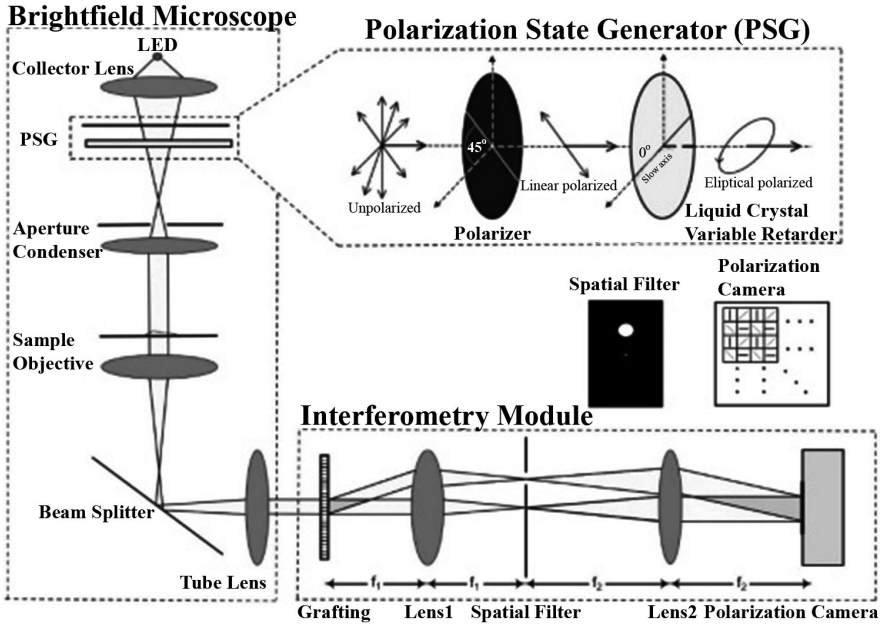

(a)

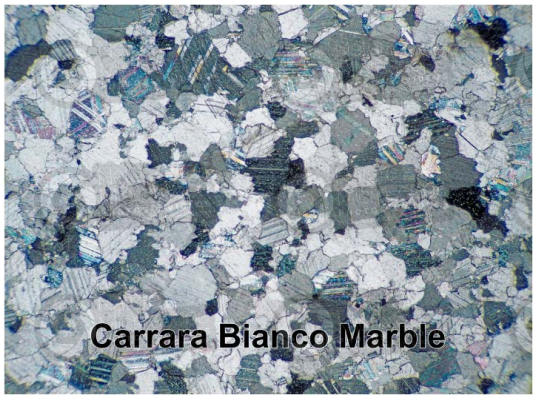

(b)

Figure 15. (a) Polarized light microscope, (b) an exemplary image [19].

3. Classification of Past Studies on Marble

3.1. Studies on Crack Propagation in Marble under Stress—Mechanical and Fracture Properties of Marble

In this paper, we have reviewed the literature for past studies on "crack propagation in marble under stress—mechanical and fracture properties of marble" and each study is compiled and exhibited in Table 4 based on materials, testing setups, test specimens, test parameters and research techniques.

Table 4. Studies on crack propagation of marble under force and investigation of mechanical and fracture properties of marble.

MATERIALS	TEST SETUP	TEST SAMPLES	FRACTURE/FLAW	INVESTIGATION TECHNIQUE	REF.
Carrara marble	Uniaxial	152 × 76 × 38 mm	127 mm length, 1 mm width, oriented at 30˚ from the horizontal axis	Atomic force microscopy (AFM), Environmental scanning electron microscopy (ESEM)	[13]
Marble/in Tibet	Uniaxial	Ø50 mm, h: 100 mm	interbed orientation of 0˚, 30˚, 60˚ and 90˚ and natural fractures	X-ray phoenix NDT analyzer micro-Computed Tomography (CT)	[20]
White marble/China and PMMA specimens	Uniaxial	Length: 110 mm Width: 50 mm Thickness from 10 mm to 50 mm	20˚, 45˚, 75˚ the inclination surface flaw 14 mm/22mm. The flaw depth 3.2 mm. PMMA specimens were frozen in a cooler containing dry ice. The rock specimen's temperature dropped to about −72˚C. Specimen testing temperature does not rise above −50˚C.	Linear Variable Differential Transformer (LVDT). Video camera.	[21]
Marble/in Tibet	Uniaxial	Ø50 mm, h: 100 mm	interbed orientation of 0˚, 30˚, 60˚, and 90˚, natural fractures	Acoustic Emission (AE) Computed Tomography (CT)	[22]
Samples composed of spherical particles with great stiffness. ρ: 2700 k·gm^{-3} R: 0.5 - 0.8 mm E_c: 37 GPa M: 0.65 k^n/k^s: 2.5	Triaxial	50 × 50 × 100 mm	The flaws inclination angles; 30˚, 60˚, 75˚ Flaw length: 24 mm 45˚ Flaw length: 20, 16, 24 mm	3-D particle-based discrete element methodology (DEM)	[23]
ρ: 2700 kg/m^3 (Density) R: 0.5 - 0.83 mm E_c: 50 GPa (Particle-contact Young Modules) M: 0.7 (Friction coefficient) k^n/k^s: 2 (Particle-contact stiffness ratio)	Biaxial	100 × 100 mm	Elliptical crack in the center, long: 10 mm	Discrete Element Methodology (DEM)	[24]

Continued

Marble/in Tibet	Uniaxial	Ø50 mm, h: 100 mm	interbed orientation of 0˚, 30˚, 60˚ and 90˚ and natural fractures	Scanning Electron Microscopy (SEM) Linear Variable Differential Transformer (LVDT)	[25]
Baishan Formation marble/China	Triaxial	100 × 100 × 200 mm	Fractures with a length Greater than 0.5 times of the specimen height. The total length of these fractures R_{11}: 429 mm R_{14}: 1370 mm	High-Speed Camera Acoustic Emission Scanning Electron Microscopy (SEM) Linear Variable Differential Transformer (LVDT)	[26]
Baishan Formation marble/China	Biaxial	50 × 50 × 100 mm	Between 60˚ and 90˚ natural fractures	Acoustic Emission (AE) Moment Tensor (MT)	[27]
White marble/China	Three-point bending	Notched semi-circular bend marble. Ø50 mm, Thicknees: 25 mm	Fracture length: 5 mm	Three-Dimensional (3D) Laser Scanner	[28]
Marble/China	Uniaxial	Ø50 mm, h: 100 mm	interbed orientation of 0˚, 30˚, 60˚ and 90˚ and natural microcracks	X-ray Computed Tomography (CT) Scanning Linear Variable Differential Transformer (LVDT)	[29]
Mainly white, partially blackish marble/China	Uniaxial	20 × 10 × 2 mm defective sample 15 × 4 × 2 mm intact sample	45˚ transparent crack	Scanning Electron Microscopy (SEM)	[30]
Marble	Uniaxial and triaxial	Ø50 mm, h: 100 mm		TAW-2000D Data Acquisition System	[31]
White marble	Uniaxial-biaxial	110 × 110 × 30 mm	45˚ double pre-existing cracks length: 20 mm, width: 1 mm	High Speed Camera	[32]
White marble/China	Three-point bending	Notched semi-circular bend marble. Ø50 mm, Thicknees: 25 mm	Fracture length: 5 mm crack width < 20 mm	High Speed Camera	[33]
White dolomitic marble/China	Triaxial	Ø50 mm, h: 100 mm	interbed orientation of 0˚, 30˚, 60˚ and 90˚ and crack pattern is simple and single	X-ray Computed Tomography (CT) Scanning Energy Mechanism Analysis	[34]
Marble/China	Uniaxial and triaxial	Ø50 mm, h: 100 mm	Natural flaws (cracks)	Acoustic Emission (AE) Linear Variable Differential Transformer (LVDT)	[35]
Marble/China	Uniaxial	50 × 100 mm rectangular	Inclination angle 0˚, 15˚, 30˚, 45˚, 60˚, 75˚, 90˚ / Flaw length 10 mm	Acoustic Emission (AE) Particle Flow Code (PFC) based on Discrete Element Method (DEM)	[36]

Continued

Carrara marble	Uniaxial and biaxial	76 × 152 mm rectangular Ø76 mm Brazilian disc model	Flaw inclination angle for single flaws 0˚, 30˚, 60˚ a flaw in the center Flaw inclination angle for En-echelon flaws 30˚, 45˚, 60˚, 75˚, 90˚ flaw length:12,5mm flaw aperture:1mm	Numerical Model Particle Flow Code (PFC)	[37]
Naturel stiff jointed marble	Triaxial	50 × 50 × 100 mm	Flaw inclination angle 62˚ - 90˚ only one natural joint plane	Scanning Electron Microscopy (SEM)	[38]
Carrara marble	Uniaxial	76 × 152 mm	En-echelon flaws inclination angle 15˚, 30˚, 45˚, 60˚, 75˚, 90˚	Particle Flow Code (PFC) Optical Microscope Video Camera	[39]
Dionysos marble	Uniaxial	40 × 40 × 100 mm	Pre-existing microcracks	Acoustic Emission (AE)	[40]
White marble	Uniaxial	60 × 60 × 30 mm	Flaw inclination angle 0˚, 30˚, 45˚, 60˚, 75˚, 90˚ flaw length: 10 mm flaw aperture: 1 - 1.5 mm	High Speed Camera	[41]
Carrara marble	Laser generated pressure waves	50 × 40 × 30 mm	Samples were taken from a strongly deteriorate tortile column removed	Laser-Based Photoacoustic Sensor	[42]
Marble/China	Uniaxial and triaxial	Ø50 mm, h: 100 mm	Microcracks	Nuclear Magnetic Imaging Resonance (NMR)	[43]
White marble	Uniaxial	Ø50 mm, h: 100 mm	Artificial flaw inclination angle 0˚, 13˚, 24˚	Acoustic Emission (AE)	[44]
Carrara marble	Uniaxial	15 × 60 × 100 mm	Flaw inclination angle 0˚, 45˚, 90˚	Digital Image Camera	[45]
Marble/China	Triaxial	50 × 50 × 100 mm	Intact and jointed marble The dip angle of the joint 0˚, 25˚, 40˚, 54˚, 60˚, 78˚	Digital Image Correlation (DIC)	[46]
Carrara marble	Uniaxial	152 × 76 × 32 mm	En-echelon flaws inclination angle 15˚, 30˚, 45˚, 60˚, 75˚, 90˚ Few intragranular micro-cracks Flaw length: 13 mm Flaw aperture: 1.2 mm	Optical Microscope and Image Recording System Linear Variable Differential Transformer (LVDT)	[47]
Bonnet granite	Uniaxial	Length to diameter ratios of approximately 2.25		Strain Gauge and Acoustic Emission (AE)	[48]
Coarse-grained Inada granite & fine-grained Oshima granite		Ø50 mm, h: 100 mm	Fractal dimensions. Inada granite: 2.3 Oshima granite: 2.7	Acoustic Emission (AE)	[49]
White Carrara marble Red Verona marble	Three-point bending	180 × 60 × 30 mm 150 × 30 × 60 mm (Large Verona marble) 150 × 30 × 30 mm (Small Verona marble)	Initial crack length 6.07 - 6.84 mm 18.80 - 19.65 mm 8.74 - 10.16 mm	Digital Image Correlation Linear Variable Differential Transformer (LVDT)	[50]

Continued

Venatino marble	Uniaxial	60 × 60 × 15 mm	Flaw inclination angle 0˚, 15˚, 30˚, 45˚, 60˚, 75˚, 90˚ Artificial flaw lengths 10, 15, 20 mm	High Speed Camera	[51]
Marble/China	Uniaxial	Ø50 mm, h: 100 mm	Natural irregular microcracks	Acoustic Emission (AE) Linear Variable Differential Transformer (LVDT)	[52]
Marble	Triaxial	Ø50 mm, h: 100 mm	Natural flaws (cracks)	X-ray Computed Tomography (CT) Scanning	[53]
Marble/China	Triaxial	Ø36.56 - 36.68 mm, h: 58.65 - 74.08 mm	pre-existing microcracks	Ultrasonic Linear Variable Differential Transformer (LVDT)	[54]
Marble/China	Uniaxial	Ø 50 mm, h: 100 mm	Flaw inclination angle 30˚, 45˚, 60˚ Flaw thickness: 0.3 - 0.5 mm Flaw length: 24 mm	Linear Variable Differential Transformer (LVDT)	[55]
Carrara marble	Uniaxial	152 × 76 × 32 mm	Flaw inclination angle 30˚, 90˚ Flaw length: 12.5 mm Flaw aperture: 0.5 mm	Scanning Electron Microscopy (SEM) Optical Microscope High Speed Camera	[56]
Plaster model Veria-Nefeli marble Volakas II marble Volakas Ariston, I marble	Uniaxial	150 × 150 × 40 mm 150 × 150 × 50 mm 200 × 200 × 80 mm 300 × 300 × 85 mm	Cured for 96 h at 40˚C, Hole of 28 mm diameter Ø10, 22, 35 and 45 mm Ø10, 22, 35 and 45 mm Ø10, 22, 35, 45 and 61 mm	Digital Image Corelation Ultrasonic Acoustic Emission (AE) Linear Variable Differential Transformer (LVDT)	[57]
Dionysos marble	Uniaxial	40 × 40 × 100 mm	Natural flaws (cracks)	Acoustic Emission (AE)	[58]
Carrara marble	Uniaxial	60 × 30 × 20 mm	Flaw inclination angle 0˚, 15˚, 30˚, 45˚, 60˚, 75˚, 90˚ Flaw length: 5 mm Flaw aperture: 1 mm	High Speed Video System	[59]
White Marble/China	Uniaxial	Ø50 mm, h: 100 mm	circumferential surface pre-crack Flaw width: 2 mm Flaw aperture: 3 mm	Acoustic Emission (AE) Linear Variable Differential Transformer (LVDT)	[60]
Grey coarse meta crystal marble	Uniaxial	Ø50 mm, h: 100 mm	natural fractures (cracks) (flaws)	Linear Variable Differential Transformer (LVDT)	[61]
Silt-crystal marble	Uniaxial and triaxial	Ø49.6 mm, h: 100 mm	Weathered marble, no imperfections is observed with naked eyes.		[62]

Table 4 shows us that studies in the subject area actively made use of research techniques such as AFM, ESEM, SEM, DEM, CT, LVDT and AE. General results obtained from studies conducted for different axes, marble sizes and crack types can be summarized as below.

Fracture process for each individual marble specimen under different loading and unloading conditions begins with the formation of a distinct damage zone around the crack tip. Subsequently, beginning from the crack tip, the damage zone gradually turns into macroscopic cracks. The cracks propagate and com-

bine. Lastly, rock pieces begin to fall off, the specimen loses its load-carrying capacity and eventually perishes completely [32].

Cracks formed under different loading and unloading conditions can be broadly classified as wing cracks, secondary planar cracks and secondary inclined cracks. In the case of uniaxial loading, the specimen contains many shear cracks and few tension cracks. Whereas in the case of biaxial loading, most cracks are shear cracks and occurrence of tensile cracks is rare [34].

Tensile and shear cracks are two different types of cracks involved in the connection process of gradual fractures, as in fault lines. Shear cracks usually occur earlier than tensile cracks and dominate the crack propagation process. However, in static tests, the cracking process is dominated by tensile cracks [41]. When the specimen reaches 78.2% of the peak tension, the critical tensile crack is in its initial stage and the macro fracture actually occurs after the peak tension [45].

The entire cracking process of defective marbles under dynamic loading can be classified into four main stages: white patches; first shear cracks; secondary tensile and shear cracks; and a combination of macro cracks until eventual failure [51]. Two types of white patches are observed; namely linear and scattered white patches. Linear white patches, which usually develop in the tensile stress concentration area, look markedly different from the surrounding-colored area. A fine-striped crack, which usually develops along the linear white patch, would later develop as an open crack. In contrast, scattered white patches, which develop in the compressive stress concentration area, exhibits an indistinct boundary with the surrounding area. It suddenly develops as a macro-crack around the peak stress [47].

In Carrara marble, a tensile fracture is characterized by a linear white patch, while a shear fracture is characterized by a scattered white patch. Both shear white patches and tensile white patches are observed before the occurrence of macro-scale shear and tensile cracks. Shear cracks usually occur earlier than tensile cracks, causing the defective specimen to ultimately break with an X-shaped shear zone. Tensile cracks usually develop with a flaw inclination angle (β) of less than 60 degrees. The development of tensile cracks is often limited by the predominant propagation of shear cracks and cannot fully develop into visible open tensile cracks. On the other hand, tensile patches that develop under semi-static loads clearly appear earlier than shear patches [59].

The damage zone of a tensile fracture includes microcracks with one or more long, dominant, wide elongation deformations surrounded by several microcracks confined within about 300 - 1000 μm (2 - 6 calcite particles). However, in the damage zone of a shear fracture, long dominant microcracks are not observed before fracture [56]. The peak stress and the corresponding strain of defective specimens are lower than those of intact specimens under dynamic loading, and these two parameters generally increase with defect inclination angle while decreasing with defect length.

In addition, in most marble specimens that are under biaxial compression, tension decreases successively until instability occurs. Stress is reduced several

times. Moreover, in some cases, stress reduction begins even before it reaches its peak value. Loading speed or strain rate has been proven to affect cracking processes [27]. Increased dynamic loading or cyclic loading leads to an increase in crack density. Cyclic loading includes the processes of blasting vibration, drilling, rock cutting, earthquake, excavation, freezing-thawing and hydraulic fracturing [20].

3.2. Studies on the Effects of Freezing and Thawing on the Mechanical Properties of Marble

In this paper, we have reviewed the literature for past studies on "the effects of freezing and thawing on the mechanical properties of marble" and each study is compiled and exhibited in Table 5 based on materials, testing setups, test specimens, test parameters and research techniques.

Table 5 shows us that studies in the subject area actively made use of research techniques such as CT, LVDT and AE. General results obtained from studies conducted for different axes, marble sizes and crack types can be summarized as below.

Studies show that marble specimens are greatly affected by freeze-thaw (F-T) treatment. As the number of F-T cycles increases, less tensile cracks occur, and more shear/mixed cracks are seen [64]. CT scans show that a complex crack network may occur for a marble specimen subjected to a low freeze-thaw process, and as the F-T cycle grows, the scale of stress cracks decreases, and shear/mixed cracks increase.

Under freeze-thaw conditions, a 9% volumetric expansion occurs when the water turns into ice, and freezing pressure fuels the development of new microcracks in the marble. Cracking speed increases with the increase in temperature and/or relative humidity [64].

Table 5. Studies on the effects of freezing and thawing on the mechanical properties of marble.

MATERIALS	TEST SETUP	TEST SAMPLES	FREEZE-THAW	INVESTIGATION TECHNIQUE	REF.
Marble/China	Uniaxial Multi-Level Cyclic Loading	Ø50 mm, h: 100 mm	Freeze-thaw treatments of 0, 20, 40 and 60 cycles 8 h under −40˚C 8 h at a room temperature 20˚C Vacuum saturation treatment for 24 h.	Linear Variable Differential Transformer (LVDT) Acoustic Emission (AE) Computed Tomography (CT) Scanning	[63]
Marble/China	Multi-level fatigue loading	Ø50 mm, h: 100 mm	Vacuum saturation treatment for 24 h. Freeze-Thaw cycles of 0, 20, 40, and 60. 8 h under −40˚C 8 h at a room temperature.	Linear Variable Differential Transformer (LVDT) Scanning Electron Microscopy	[64]
Carrara marble		10 cm square plates	25 freeze-thaw cycles for temperatures (100˚C, 200˚C, 300˚C and 400˚C). Thaw cycles for 30 min a recipient with ice cube are used.	Ultrasonic Laser Vibrometer	[65]

Previous F-T damage greatly affects the mode of cracking. It is argued that tensile cracking mode plays a dominant role for marble specimens not subjected to the freeze-thaw process, and shear cracking mode is for marble specimens subjected to high F-T process. As the number of F-T cycles increases, less tensile cracks occur and more shear/mixed cracks are seen [63].

3.3. Studies on the Effects of Water Saturation on Mechanical Properties and Fracture Behavior of Marble

In this paper, we have reviewed the literature for past studies on "the effects of water saturation on mechanical properties and fracture behavior of marble" and each study is compiled and exhibited in Table 6 based on materials, testing setups, test specimens, test parameters and research techniques.

Table 6 shows us that studies in the subject area actively made use of research techniques such as CT and LVDT. General results obtained from studies conducted for different axes, marble sizes and crack types can be summarized as below.

Wet marble can be up to 40% weaker than dried marble. It can be argued that such difference in strength is due to expansion that increases the high pore fluid pressure and due to the help of grain boundary shift (GBS) in contributing to creep [67].

The effect of water on the strength of calcite marble at high temperature is small. For instance, the strength difference between wet and dry marble at 700˚C is less than that at lower temperatures and does not exceed 10% on average.

Table 6. Studies on the effects of water saturation on the mechanical and fracture properties of marble.

MATERIALS	TEST SETUP	TEST SAMPLES	FREEZE-THAW	INVESTIGATION TECHNIQUE	REF.
Carrara marble	Triaxial	Ø5 mm, h: 10 mm	Int he range 23˚C - 25˚C First sample dry. Second sample wet. The sample was saturated in water under vacuum for 24 hr before the experiment.	Linear Variable Differential Transformer (LVDT) Dynamic X-Ray Microcomputed Tomography Imaging (4- D XCT)	[66]
Carrara marble	Axially compressed	Ø10 mm, h: 20 mm	Dry; temperatures ranging 600˚C - 1000˚C. Wet; addition of 0.4% - 2.1% water.	Light Optical Polarization Microscope Scanning Electron Microscope (SEM)	[67]
Calcitic marble	Pulsed React or IBR-2	Ø15 mm, h: 50 mm	Dry Conditions; Heating and cooling rate 0.5˚C/min 60˚C in cycle 1 and 90˚C in cycle 2 and 3 One hour before the heating -up of each cycle the climate chamber was filled with water Temperature 90˚C was kept for 8 h.	Displacement Sensor	[68]

The bending of calcite marble panels should be considered as irreversible expansion of the rock under the effect of temperature changes and humidity. Humidity is considered as a key parameter related to the phenomenon of bending and can lead to unlimited residual expansion in certain types of marble. In general, if the panel is exposed to sunlight and high humidity only from the outside, it starts to bend outwards; whereas if there is moisture behind the panel in a confined space where relative humidity is close to 100%, it starts to bend inwards [68].

It is still unclear how moisture combined with temperature cycles (day-night) causes marble to deteriorate. It is assumed that average wind speed is the primary factor that causes flexural differences.

3.4. Studies on the Effects of Temperature on the Micro-Structure and Physico-Mechanical Properties of Marble

In this paper, we have reviewed the literature for past studies on "the effects of temperature on the micro-structure and physico-mechanical properties of marble" and each study is compiled and exhibited in Table 7 based on materials, testing setups, test specimens, heat treatment and research techniques.

Table 7. Studies on the effects of temperature on the microstructure and physico-mechanical properties of marble.

MATERIALS	TEST SETUP	TEST SAMPLES	THERMAL TREATMENT	INVESTIGATION TECHNIQUE	REF.
Greek and Turkish marble	Uniaxial	Cubic specimens of 50 mm side length	100˚C, 200˚C, 300˚C, 400˚C for one hour	Ultrasonic Polarizing light microscope X-ray diffraction	[69]
Carrara marble/ in Italy	Uniaxial and triaxial	Cylindrical specimens	Maximum temperature 600˚C, 12 hours of heating and cycles.	Pressure Sensors	[70]
Dolomitic marble/China	Uniaxial	Ø50 mm, h: 100 mm	600˚C with a heating rate of 10˚C/min.	Optical Microscope	[71]
Marble/China	Uniaxial	Ø50 mm, h: 100 mm	20˚C, 400˚C, 600 ˚C for 4 hours	Acoustic Emission	[72]
Carrara marble/ in Italy Macedonian marble	Uniaxial	45 × 140 × 3 mm	Influence of temperature Low temperature 293 K, humidity 47% - 50% Intermediate temperature 323 - 324 K, humidity 50% High temperature 351 K, humidity 50% Influence of relative humidity Low humidity 5% - 7%, 323 K Intermediate humidity 50%, 323 - 324 K High humidity 89% - 92%, 323 - 324 K	Optical-Digital Microscope	[73]
Mugla marble/Turkey	Uniaxial	Ø54 mm, h: 108 mm	24 h/400˚C Cycle heating-cooling 24 h/−24˚C Cycle of freeze-thaw	Ultrasonic	[74]
Marble/China	Uniaxial	Ø50 mm, h: 100 mm	Room Temperature, 100˚C, 200˚C, 400˚C, 600˚C, 800˚C, 1000˚C, heating rate of 10˚C/min. Once reached, is kept Constant for 2 h.	Pressure sensor	[75]

Continued

Marble/ China	Uniaxial and triaxial	Ø50 mm, h: 100 mm	200˚C, 400˚C, 600˚C for a period of 4 h, heating rate of 10˚C/min. Once reached, is kept Constant for 4 h.	Polarizing Microscopy Ultrasonic	[76]
Marble/ China	Uniaxial	Ø50 mm, h: 100 mm	Room Temperature (25˚C), 200˚C, 400˚C, 600˚C, heating rate of 10˚C/min. Once reached, is kept Constant for 4 h.	Ultrasonic Pulse transmission technique	[77]
Marble/ China	Uniaxial	Ø25, 50, 75 and 100 mm specimens have a length to diameter ratio of 2.	Room Temperature (25˚C), 200˚C, 400˚C, 600˚C, heating rate of 10˚C/min. Once reached, is kept Constant for 4 h.	Ultrasonic Pulse transmission technique	[78]
Off-white colour marble/China	Uniaxial	Ø100 mm, h: 50 mm	25˚C, 100 ˚C, 200˚C, 400˚C, 600˚C, 800˚C and 1000˚C, heating rate of 10˚C/min. Once reached, is kept Constant for 3 h.	Split Hopkinson Pressure Bar Device	[79]
Muğla marble/Turkey	Uniaxial	Ø54 mm, h: 110 mm	400˚C ≥ thermal treatment In water for a duration of 24 h. 24 h for each thermal cycle. (1/2, 1, 2, 3, 4, 8 cycles)	Linear Variable Differential Transformer (LVDT)	[80]
Black marble/Italy Whitish-pink limestone/Italy	Uniaxial	Cubic about 70 mm edge specimens	230˚C, 400˚C, 500˚C 400˚C, 470˚C, 600˚C Heating rate of 2.4˚C/min. Cooling rate of 0.23˚C/min.	Ultrasonic Polarising Optical Microscope	[81]
Marble/Greece		185 × 35 × 20 mm	The humidity ranges 18% - 85%, 72˚C - 22˚C, 95 cyles The humidity ranges 50%, 80˚C - 25˚C, Temperature from 25 to 80 over 200 of 3 h.	Scanning Electron Microscopy (SEM)	[82]
White macael marble Tranco macael marble Yellow macael marble/Spain			20˚C → 45˚C → 90˚C returns to 20˚C. heating rate of 1˚C/min. 3 dry cycles and 7 wet cycles, 10 cycles in total 15 h in dry Conditions, 17 h in wet Conditions.	Hot stage Scanning Electron Microscopy Ultrasound Mercury Intrusion Porosimetry	[83]
Five well-known marble lacations: Carrara/Turkey/ Rosa Estremos/ Wachau/ Wunsiedel		Cuboid 10 × 10 × 50 mm	80˚C ≥ upper Temperature limit only one heating/cooling cycle	Linear Variable Differential Transformer (LVDT)	[84]

Table 7 shows us that studies in the subject area actively made use of research techniques such as SEM, LVDT, AE and UT. General results obtained from studies conducted for different axes, marble sizes and heat treatment methods can be summarized as below.

Environmental temperature fluctuations create new microcracks in marble and cause existing ones to expand, resulting in an increase in porosity, which is the first stage of decay. It has been shown that numerous factors contribute to marble erosion due to thermal changes. These include mineralogical composi-

tion of marble, its grain size and shape, texture and type of junction between crystals [83].

The effects of heating on two different marble specimens are not the same. For example, the volume increase in black marble (consisting of crystallized calcite) with heating is due only to new fracture formations, while in white marble (consisting of microcrystalline calcite) heating causes minor deterioration and a larger increase in volume (55%). The effects of heating are determined by the mineralogical and textural properties of the marble. For crystalline marble specimens (black marble), formation of new cracks is much more important than matrix distortion, whereas the opposite is true for micritic limestone (white marble). In addition, thermal expansion causes more damage in calcite marbles than in dolomite marbles [81].

When a marble specimen is heated to 200˚C, 400˚C and 600˚C and subsequently cooled to room temperature (25˚C), its color changes considerably due to exposure to high temperatures and many microcracks occur in the marble [78]. As the applied temperature increases, longitudinal wave velocity, uniaxial compressive strength and Young's modulus gradually decrease and the peak stress corresponding to the peak force increases [77].

It was discovered that P wave velocity decreases with the increase in process temperature, and effective porosity increases with process temperature. It was also found that Poisson's ratio gradually increases with temperature [72].

Temperature changes from room temperature to up to 60˚C have no significant effect on tension-strain curves. However, when temperature reaches 800˚C, the stress-strain curve is concave [75].

The largest expansion and the largest separation between grain boundaries occur at 90˚C temperature. Thermal decomposition at temperatures above 200˚C has been found to cause formation of significant microcracks in marble [84]. It has been found that the number of thermally-induced microcracks grows significantly with the increase in the number of heating and cooling cycles. However, it was determined that the width and length of such microcracks increase substantially with the increase in the number of heating and cooling cycles [71].

A rise in process temperature gradually increases the effective porosity and total porosity while significantly decreasing the ultrasonic P wave velocity, which indirectly reflects thermal cracking [76]. In addition, the velocity of ultrasonic pulses moving in marble depends on properties such as density, texture, anisotropy, saturation, temperature and elasticity, as well as porosity and pore size [74]. The directional dependence of the total size of the thermal expansion coefficient and permanent deformation is highest in marbles with strong texture, while Carrara marble with weak texture exhibits a uniform crack formation [84].

In general, strength properties and acoustic and thermal conductivity of marble gradually decrease with the increase in temperature, while permeability and electrical conductivity increase instead [76]. In addition, heating increases duc-

tility to a certain extent.

3.5. Studies on Determination of Discontinuities in Marble Sites

In this paper, we have reviewed the literature for past studies on "determination of discontinuities in marble sites" and each study is compiled and exhibited in Table 8 based on materials, observation depth, test specimens and research techniques.

Table 8 shows that the GPR research technique has been actively used in studies in this field. General results obtained from the studies conducted in different regions, depths and areas can be summarized as follows.

Uncontrolled discontinuities in marble quarries are the main factor that reduces efficiency. There is no way to change them. However, if the thickness of the marble to be extracted from the potential quarry and frequency distances of the discontinuities (fractures, cracks, cavities) it contains are determined prior to the opening of the marble surface (mirror), this would significantly reduce operating costs and unforeseen losses. In such case, it is estimated that a block efficiency of 10% and more can be obtained from the 1st region, 5% to 10% from the 2nd region less than 5% from the 3rd region. In addition, it was determined by studies that the commercial size block volumes that can be extracted from regions 1 and 2 would vary between 1.20 m^3 and 7.90 m^3 [86].

3.6. Studies on Crack Assessment in Marble Sculptures

In this paper, we have reviewed the literature for past studies on "crack assessment in marble sculptures" and each study is compiled and exhibited in Table 9 based on materials, testing setups, test specimens, heat treatment and research techniques.

Table 8. Studies on the determination of discontinuities in the marble sites.

MATERIALS	VISUALISATION DEPTH	TEST SAMPLES	INVESTIGATION TECHNIQUE	REF.
Limstone Sivas province, Gürün district /Turkey	4.5 - 5 m	100 m × 100 m	GPR (RAMAC Cu II) 100 MHz closed System antennas. 21 profile lines were determined at 5 m intervals along 100 m. Measurements were taken at 10 cm intervals in each profile.	[85]
Beige marble Burdur province, Hacılar village /Turkey	25 - 30 m	4 hectares	GPR 38 MHz 50 m long lines have been determined. Simultaneous images were obtained on the computer with the antenna held approximately 25 - 30 cm above the ground on these determined lines.	[86]
Sivas/Gürün Ankara/Polatlı Kırşehir/Akpınar Adıyaman Ankara/Gölbaşı Marble/Turkey		3 m × 3 m blocks	GPR 100 MHz and 250 MHz closed system antennas. 1600 MHz	[87]

Table 9. Studies on crack assessment in marble sculptures.

MATERIALS	TEST SETUP	TEST SAMPLES	THERMAL TREATMENT	INVESTIGATION TECHNIQUE	REF.
Michelangelo's David in Florance		5.16 m high nearly 6 ton three different path lengths of 60 mm, 70 mm and 80 mm	Natural Temperature variations and wetting-drying cycles	Ultrasonic (55 kHz) maximum depth 20 mm	[88]
Proconnesus marbleThasos Island/Greece Graeco-Roman style and date to the Roman period		The piece is 99.1 cm high, 35 cm wide and 31.5 cm thick. The height of the piece is 79 cm, width 56 cm, thickness39 cm. The hight of the piece is 97 cm, width 41 cm, thickness 37 cm. 130 cm high, 63 cm wide and 33 cm thick. 89 high, 41 cm wide, 31 cm thick.	visible surface cracks	Ultrasonic (250 kHz) Optical Microscopy X-ray diffraction for distances up to 20 cm	[89]
Neuer Garten, Potsdam/Germany, Prie born Marble obelisk		Square ground plan and narrows from the bottom up, height: 5.2 m, the faces of the profiled plinth are within 1.2 degrees off the vertical.	Prieborn marble cube 65 mm, to analyzer the progressive deterioration of this marble subsequently 60˚C, 90˚C, 150˚C, 200˚C heated and cooled down.	Ultrasonic (46 kHz) Analyzer Microscope	[90]
The sculpture Mercury and Psyche from Reinhold Begas, Berlin/Germany		Marble cube edge length of 10 cm		Ultrasound Image, maximal penetration depth of 50 cm X-Ray Diffraction, maximal penetration depth of 20 cm	[91]
Naturally sugaring marbles from Monumental Cemetery in Bologna/Italy And Carrara marble		12 × 9 × 3 cm Rectangular 30 × 30 × 10 mm Prismatic	Samples were produced at 400˚C for 1 h.	Electron Microscopy Mercury Intrusion Porosimetry Ultrasonic (55 kHz)	[92]

Table 9 shows that the UT research technique has been actively used in studies in this field. The general results obtained from the studies carried out for different axes, sculpture types and heat treatment methods can be summarized as follows.

The so-called "granulation" of marble is a very common phenomenon of deterioration which results from environmental temperature fluctuations and affects historical monuments and modern buildings alike. Thermal cycles are in fact responsible for the formation of microcracks at the boundaries between calcite grains, which expose the marble to granular fragmentation [92].

Degradation of marble is mainly related to the excessive anisotropic thermal expansion of carbonate crystals [90]. Artificially eroded specimens produced by heating fresh Carrara marble at 400˚C for 1 hour exhibit widespread microcracks at grain boundaries, just like naturally decomposed samples.

The most frequently used technique in these studies is the measurement of

the velocity of longitudinal ultrasonic waves via the direct transmission method. What various ultrasound techniques all have in common is the utilization of a single-channel electronic system with transmitting and receiving transformers having frequencies lower than 350 kHz. Measurements are time-consuming and the locations or dimensions of internal defects can only be estimated [91].

It was determined that microcracking and increased porosity in marble sculptures result in the ultrasonic pulse rate to decrease from 5.1 to 1.9 km/h after heating. A decrease in V_p can be explained by an increase in porosity. Further, the V_p velocity is also dependent on the mineralogical, physical and mechanical properties of marble, the degree of water saturation and the level of degradation. These minor changes in the pore structure of the sculptures are eliminated by consolidating with hydroxyapatite, which provides good durability in terms of resistance to thermal weathering, salt crystallization cycles and F-T cycles. V_p velocity can thereby be increased from 1.9 km/h to 3.6 km/h. The most alarming cracks in sculptures occur in the "broncone," which is defined as the trunk of the right leg [88].

4. Discussion

Determination of weak zones, discontinuities and mineral structure significantly improves production efficiency by eliminating marble waste during the extraction from the quarry, transportation and processing phases. The richest marble deposits in the world are found in countries such as Turkey, Italy, Spain, Greece, the Netherlands, China and Egypt, which are located in the Alpine belt. For example, Turkey ranks first in raw marble exports and third in processed marble exports, after China and Italy. Therefore, the high marble production efficiency would increase the economic return for these countries. An increase in production efficiency would be possible by minimizing the amount of marble waste and maximizing the amount of processed marble. Increase in processed marble has a positive effect not only on the products related to the construction sector, but also on the creation of artistic products such as ornaments-decoration and sculptures. This would trigger an increase in exports in such direction, thereby strengthening the country's economy.

5. Conclusion

Gaining knowledge on the developments in all processes, from the extraction of marble to its transformation into products, would also contribute to the reduction of marble waste and improvement of production efficiency. This study therefore has reviewed and classified past academic studies on marble in 6 main categories, with the aim of keeping the production efficiency of marble, a metamorphic rock, within the economic limit values. Each category was compiled and presented in tables based on materials, testing setups, test specimens, test parameters and research techniques, and the general results for each category

were subsequently provided. In the light of said results, new techniques and new approaches can be determined in order to reduce marble waste. We believe that this study will provide faster and more accurate solutions by guiding researchers working in this field.

Conflicts of Interest

The authors declare no conflicts of interest regarding the publication of this paper.

References

[1] Zhu, Z.N., *et al.* (2018) Effects of High Temperature on the Mechanical Properties of Chinese Marble. *Rock Mechanics and Rock Engineering*, **51**, 1937-1942. https://doi.org/10.1007/s00603-018-1426-0

[2] Demir, B.G. and Güngör, N. (2013) Marble Mining & Environment. *Journal of Istanbul Aydin University*, **5**, 7-14. https://dergipark.org.tr/en/pub/iaud/issue/30067/324585

[3] Küçük, K. and Onargan, T. (2018) Block Efficiency Evaluation in Burdur Beige Marble Quarry with Ground Radar (GPR) Method. *Fırat University Journal of Science*, **30**, 51-59. https://dergipark.org.tr/en/pub/fufbd/issue/35839/400753

[4] Ugur, I., Sengun, N., Demirdag, S. and Altindag, R. (2014) Analysis of the Alterations in Porosity Features of Some Natural Stones Due to Thermal Effect. *Ultrasonics*, **54**, 1332-1336. https://doi.org/10.1016/j.ultras.2014.01.013

[5] Vasanelli, E., Colangiuli, D., Calia, A., Sileo, M. and Aiello, M.A. (2015) Ultrasonic Pulse Velocity for the Evaluation of Physical and Mechanical Properties of a Highly Porous Building Limestone. *Ultrasonics*, **60**, 33-40. https://doi.org/10.1016/j.ultras.2015.02.010

[6] Fallahi, N., Nardoni, G., Heidary, H., Palazzetti, R., Yan, X.T. and Zucchelli, A. (2016) Supervised and Non-Supervised AE Data Classification of Nanomodified CFRP during DCB Tests. *FME Transactions*, **44**, 415-421. https://doi.org/10.5937/fmet1604415F

[7] Shin, D.-J., Kang, W.-S., Lim, D.-H., Koo, B.-K., Kim, M.-S., Jeong, S.-J. and Kim, I.-S. (2021) Lead-Free AE Sensor Based on BZT–BCT Ceramics. *Sensors*, **21**, Article No. 7100. https://doi.org/10.3390/s21217100

[8] Bicakci, S., Citak, H., Gunes, H., Coramik, M., Aydın, Y. and Ege, Y. (2023) Discontinuity Detection System in Marble: Analysis of the Time-Frequency Characteristics of Ultrasonic P-Waves. *Journal of Testing and Evaluation*, **51**, Article ID: 20220415.

[9] Wang, Y., Feng, W.K., Wang, H.J., Han, J.Q. and Li, C.H. (2019) Geomechanical and Acoustic Properties of Intact Granite Subjected to Freeze-Thaw Cycles during Water-Ice Phase Transformation in Beizhan's Open Pit Mine Slope, Xinjiang, China. *Water*, **11**, Article No. 2309. https://doi.org/10.3390/w11112309

[10] Martino, M., Danisi, A., Losito, R., Masi, A. and Spiezia, G. (2010) Design of a Linear Variable Differential Transformer with High Rejection to External Interfering Magnetic Field. *IEEE Transactions on Magnetics*, **46**, 674-677. https://doi.org/10.1109/TMAG.2009.2033341

[11] Santhosh, K.V. and Roy, B.K. (2017) Online Implementation of an Adaptive Calibration Technique for Displacement Measurement Using LVDT. *Applied Soft Computing*, **53**, 19-26. https://doi.org/10.1016/j.asoc.2016.12.032

[12] Liu, L., Wu, S., Pang, H., Hu, X. and Hu, X. (2019) High-Speed Atomic Force Microscope with a Combined Tip-Sample Scanning Architecture. *Review of Scientific Instruments*, **90**, Article ID: 063707. https://doi.org/10.1063/1.5089534

[13] Brooks, Z., Ulm, F.J. and Einstein, H.H. (2013) Environmental Scanning Electron Microscopy (ESEM) and Nanoindentation Investigation of the Crack Tip Process Zone in Marble. *Acta Geotechnica*, **8**, 223-245. https://doi.org/10.1007/s11440-013-0213-z

[14] Zaefferer, S. (2011) A Critical Review of Orientation Microscopy in SEM and TEM. *Crystal Research and Technology*, **46**, 607-628. https://doi.org/10.1002/crat.201100125

[15] Tan, J., Xie, J., Li, L., Lyu, Q., Han, J. and Zhao, Z. (2020) Multifractal Analysis of Acoustic Emissions during Hydraulic Fracturing Experiments under Uniaxial Loading Conditions: A Niutitang Shale Example. *Geofluids*, **2020**, Article ID: 8845292. https://doi.org/10.1155/2020/8845292

[16] Jiang, S., Tang, C., Li, X., Tan, Y., Peng, R., Yang, D. and Liu, S. (2020) Discrete Element Modeling of the Machining Processes of Brittle Materials: Recent Development and Future Prospective. *The International Journal of Advanced Manufacturing Technology*, **109**, 2795-2829. https://doi.org/10.1007/s00170-020-05792-y

[17] De Graaf, R.A. (2019) *In Vivo* NMR Spectroscopy: Principles and Techniques. John Wiley & Sons, Hoboken, 584 p. https://doi.org/10.1002/9781119382461

[18] Bond, L.J. (1991) Laser Ultrasonics: Techniques and Applications: CB Scruby and LE Drain. Adam Hilger, Bristol, 467 p.

[19] Carlton, R.A. and Carlton, R.A. (2011) Polarized Light Microscopy. In: Carlton, R.A., Ed., *Pharmaceutical Microscopy*, Springer, Berlin, 7-64. https://doi.org/10.1007/978-1-4419-8831-7_2

[20] Wang, Y., Hu, Y.Z. and Gao, S.H. (2021) Dynamic Mechanical Behaviors of Interbedded Marble Subjected to Multi-Level Uniaxial Compressive Cyclic Loading Conditions: An Insight into Fracture Evolution Analysis. *Engineering Fracture Mechanics*, **241**, Article ID: 107410. https://doi.org/10.1016/j.engfracmech.2020.107410

[21] Wong, R.H.C., Law, C.M., Chau, K.T. and Shen Zhu, W. (2004) Crack Propagation from 3-D Surface Fractures in PMMA and Marble Specimens under Uniaxial Compression. *International Journal of Rock Mechanics and Mining Sciences*, **41**, 37-42. https://doi.org/10.1016/j.ijrmms.2004.03.016

[22] Wang, Y., Meng, H. and Long, D. (2021) Experimental Investigation of Fatigue Crack Propagation in Interbedded Marble under Multilevel Cyclic Uniaxial Compressive Loads. *Fatigue & Fracture of Engineering Materials & Structures*, **44**, 933-951. https://doi.org/10.1016/j.ijrmms.2004.03.016

[23] Zhang, Y., Liu, S., Kou, M. and Wang, Z. (2020) Mechanical and Failure Characteristics of Fissured Marble Specimens under True Triaxial Compression: Insights from 3-D Numerical Simulations. *Computers and Geotechnics*, **127**, Article ID: 103785. https://doi.org/10.1016/j.compgeo.2020.103785

[24] Wang, S., Tan, F., You, M., Jiao, Y.Y. and Tu, F. (2020) Discrete Element Modeling of Crack Initiation Stress of Marble Based on Griffith's Strength Theory. *Advances in Civil Engineering*, **2020**, Article ID: 8876661. https://doi.org/10.1155/2020/8876661

[25] Wang, Y., Han, J., Ren, J. and Li, C. (2021) Anisotropic Fracture and Energy Dissipation Characteristics of Interbedded Marble Subjected to Multilevel Uniaxial Compressive Cyclic Loading. *Fatigue & Fracture of Engineering Materials & Struc-*

tures, **44**, 366-382. https://doi.org/10.1111/ffe.13365

[26] Jiang, Q., Zhang, M., Yan, F., Su, G., Feng, X., Xu, D. and Feng, G. (2021) Effect of Initial Minimum Principal Stress and Unloading Rate on the Spalling and Rockburst of Marble: A True Triaxial Experiment Investigation. *Bulletin of Engineering Geology and the Environment*, **80**, 1617-1634. https://doi.org/10.1007/s10064-020-01995-5

[27] Wang, Z., Feng, X.T., Yang, C., Zhou, Y., Xu, H., Han, Q. and Gao, Y. (2020) Experimental Investigation on Fracturing Process of Marble Under Biaxial Compression. *Journal of Rock Mechanics and Geotechnical Engineering*, **12**, 943-959. https://doi.org/10.1016/j.jrmge.2020.05.002

[28] Liu, Y., Fu, A., Jiang, B., Yu, L. and Wang, X. (2020) Study on the Static and Dynamic Fracturing Properties of Marble after Being Damaged Dynamically. *Advances in Civil Engineering*, **2020**, Article ID: 8886198. https://doi.org/10.1155/2020/8886198

[29] Wang, Y., Gao, S.H. and Han, J.Q. (2021) Fatigue-Damage Evolution Characteristics of Interbeded Marble Subjected to Dynamic Uniaxial Cyclic Loads. *Geotechnical and Geological Engineering*, **39**, 855-870. https://doi.org/10.1007/s10706-020-01526-9

[30] Tang, H.D. (2020) Multi-Scale Crack Propagation and Damage Acceleration during Uniaxial Compression of Marble. *International Journal of Rock Mechanics and Mining Sciences*, **131**, Article ID: 104330. https://doi.org/10.1016/j.ijrmms.2020.104330

[31] Fu, B. and Hu, L. (2020) Experimental and Numerical Investigations on Crack Development and Mechanical Behavior of Marble under Uniaxial Cyclic Loading Compression. *International Journal of Rock Mechanics and Mining Sciences*, **130**, Article ID: 104289. https://doi.org/10.1016/j.ijrmms.2020.104289

[32] Song, Y.Q., Li, X.S., Zhou, T. and Li, M. (2020) Experimental and Finite Element Analysis of Marble with Double Pre-Existing Flaws under Loading-Unloading Conditions. *Arabian Journal of Geosciences*, **13**, Article No. 392. https://doi.org/10.1007/s12517-020-05368-w

[33] Yu, L., Fu, A., Yin, Q., Jing, H., Zhang, T. and Qin, H. (2020) Dynamic Fracturing Properties of Marble after Being Subjected to Multiple Impact Loadings. *Engineering Fracture Mechanics*, **230**, Article ID: 106988. https://doi.org/10.1016/j.engfracmech.2020.106988

[34] Wang, Y., Feng, W.K. and Li, C.H. (2020) On Anisotropic Fracture and Energy Evolution of Marble Subjected to Triaxial Fatigue Cyclic-Confining Pressure Unloading Conditions. *International Journal of Fatigue*, **134**, Article ID: 105524. https://doi.org/10.1016/j.ijfatigue.2020.105524

[35] Liu, X., Yu, J., Zhu, Y., Yao, W. and Lai, Y. (2020) Creep Damage Evolution of Marble from Acoustic Emission and the Damage Threshold. *Frontiers in Earth Science*, **8**, Article No. 58. https://doi.org/10.3389/feart.2020.00058

[36] Zheng, L., Huang, D., Li, X. and Hu, X. (2020) Numerical Analysis of Fracture Behaviour on Marble Samples Containing Two Flaws. *Advances in Civil Engineering*, **2020**, Article ID: 6278289. https://doi.org/10.1155/2020/6278289

[37] Cheng, Y. and Wong, L.N.Y. (2020) A Study on Mechanical Properties and Fracturing Behavior of Carrara Marble with the Flat-Jointed Model. *International Journal for Numerical and Analytical Methods in Geomechanics*, **44**, 803-822. https://doi.org/10.1002/nag.3040

[38] Gao, Y., Feng, X.T., Wang, Z. and Zhang, X. (2020) Strength and Failure Characte-

ristics of Jointed Marble under True Triaxial Compression. *Bulletin of Engineering Geology and the Environment*, **79**, 891-905. https://doi.org/10.1007/s10064-019-01610-2

[39] Cheng, Y., Jiao, Y.Y. and Tan, F. (2019) Numerical and Experimental Study on the Cracking Behavior of Marble with En-Echelon Flaws. *Rock Mechanics and Rock Engineering*, **52**, 4319-4338. https://doi.org/10.1007/s00603-019-01849-x

[40] Triantis, D. and Kourkoulis, S. (2019) Fracture Precursor Phenomena in Marble Specimens under Uniaxial Compression by Means of Acoustic Emission Data. *Frattura ed Integrità Strutturale*, **13**, 537-547. https://doi.org/10.3221/IGF-ESIS.50.45

[41] Li, D., Han, Z., Sun, X., Zhou, T. and Li, X. (2019) Dynamic Mechanical Properties and Fracturing Behavior of Marble Specimens Containing Single and Double Flaws in SHPB Tests. *Rock Mechanics and Rock Engineering*, **52**, 1623-1643. https://doi.org/10.1007/s00603-018-1652-5

[42] Ciofini, D., Mencaglia, A.A. and Siano, S. (2018) A Photoacoustic Pulse-Echo Probe for Monitoring Surface Stone Mechanical Properties: Validation Tests in Consolidation of Carrara Marble. *Construction and Building Materials*, **187**, 610-619. https://doi.org/10.1016/j.conbuildmat.2018.07.225

[43] Zhou, K., Liu, T. and Hu, Z. (2018) Exploration of Damage Evolution in Marble Due to Lateral Unloading Using Nuclear Magnetic Resonance. *Engineering Geology*, **244**, 75-85. https://doi.org/10.1016/j.enggeo.2018.08.001

[44] Zhang, Z.H., Deng, J.H., Zhu, J.B. and Li, L.R. (2018) An Experimental Investigation of the Failure Mechanisms of Jointed and Intact Marble under Compression Based on Quantitative Analysis of Acoustic Emission Waveforms. *Rock Mechanics and Rock Engineering*, **51**, 2299-2307. https://doi.org/10.1007/s00603-018-1484-3

[45] Li, D., Zhu, Q., Zhou, Z., Li, X. and Ranjith, P.G. (2017) Fracture Analysis of Marble Specimens with a Hole under Uniaxial Compression by Digital Image Correlation. *Engineering Fracture Mechanics*, **183**, 109-124. https://doi.org/10.1016/j.engfracmech.2017.05.035

[46] Gao, Y. and Feng, X.T. (2019) Study on Damage Evolution of Intact and Jointed Marble Subjected to Cyclic True Triaxial Loading. *Engineering Fracture Mechanics*, **215**, 224-234. https://doi.org/10.1016/j.engfracmech.2019.05.011

[47] Cheng, Y., Wong, L.N.Y. and Zou, C. (2015) Experimental Study on the Formation of Faults from En-Echelon Fractures in Carrara Marble. *Engineering Geology*, **195**, 312-326. https://doi.org/10.1016/j.enggeo.2015.06.004

[48] Eberhardt, E., Stead, D. and Stimpson, B. (1999) Quantifying Progressive Pre-Peak Brittle Fracture Damage in Rock during Uniaxial Compression. *International Journal of Rock Mechanics and Mining Sciences*, **36**, 361-380. https://doi.org/10.1016/S0148-9062(99)00019-4

[49] Lei, X., Nishizawa, O., Kusunose, K. and Satoh, T. (1992) Fractal Structure of the Hypacenter Distributions and Focal Mechanism Solutions of Acoustic Emission in Two Granites of Different Grain Sizes. *Journal of Physics of the Earth*, **40**, 617-634. https://doi.org/10.4294/jpe1952.40.617

[50] Spagnoli, A., Carpinteri, A., Ferretti, D. and Vantadori, S. (2016) An Experimental Investigation on the Quasi-Brittle Fracture of Marble Rocks. *Fatigue & Fracture of Engineering Materials & Structures*, **39**, 956-968. https://doi.org/10.1111/ffe.12429

[51] Li, X., Zhou, T. and Li, D. (2017) Dynamic Strength and Fracturing Behavior of Single-Flawed Prismatic Marble Specimens under Impact Loading with a Split-Hopkinson Pressure Bar. *Rock Mechanics and Rock Engineering*, **50**, 29-44.

https://doi.org/10.1007/s00603-016-1093-y

[52] Li, T., Pei, X., Wang, D., Huang, R. and Tang, H. (2019) Nonlinear Behavior and Damage Model for Fractured Rock under Cyclic Loading Based on Energy Dissipation Principle. *Engineering Fracture Mechanics*, **206**, 330-341. https://doi.org/10.1016/j.engfracmech.2018.12.010

[53] Wang, Y., Li, C.H. and Hu, Y.Z. (2018) Use of X-Ray Computed Tomography to Investigate the Effect of Rock Blocks on Meso-Structural Changes in Soil-Rock Mixture under Triaxial Deformation. *Construction and Building Materials*, **164**, 386-399. https://doi.org/10.1016/j.conbuildmat.2017.12.173

[54] Liu, Z. and Shao, J. (2017) Strength Behavior, Creep Failure and Permeability Change of a Tight Marble under Triaxial Compression. *Rock Mechanics and Rock Engineering*, **50**, 529-541. https://doi.org/10.1007/s00603-016-1134-6

[55] Yang, S.Q., Dai, Y.H., Han, L.J. and Jin, Z.Q. (2009) Experimental Study on Mechanical Behavior of Brittle Marble Samples Containing Different Flaws under Uniaxial Compression. *Engineering Fracture Mechanics*, **76**, 1833-1845. https://doi.org/10.1016/j.engfracmech.2009.04.005

[56] Cheng, Y. and Wong, L.N.Y. (2018) Microscopic Characterization of Tensile and Shear Fracturing in Progressive Failure in Marble. *Journal of Geophysical Research: Solid Earth*, **123**, 204-225. https://doi.org/10.1002/2017JB014581

[57] Lotidis, M.A., Nomikos, P.P. and Sofianos, A.I. (2020) Laboratory Study of the Fracturing Process in Marble and Plaster Hollow Plates Subjected to Uniaxial Compression by Combined Acoustic Emission and Digital Image Correlation Techniques. *Rock Mechanics and Rock Engineering*, **53**, 1953-1971. https://doi.org/10.1007/s00603-019-02025-x

[58] Triantis, D., Stavrakas, I., Pasiou, E.D. and Kourkoulis, S.K. (2020) Assessing the Acoustic Activity in Marble Specimens under Stepwise Compressive Loading. *Material Design & Processing Communications*, **2**, e100. https://doi.org/10.1002/mdp2.100

[59] Zou, C. and Wong, L.N.Y. (2014) Experimental Studies on Cracking Processes and Failure in Marble under Dynamic Loading. *Engineering Geology*, **173**, 19-31. https://doi.org/10.1016/j.enggeo.2014.02.003

[60] Li, L.R., Deng, J.H., Zheng, L. and Liu, J.F. (2017) Dominant Frequency Characteristics of Acoustic Emissions in White Marble during Direct Tensile Tests. *Rock Mechanics and Rock Engineering*, **50**, 1337-1346. https://doi.org/10.1007/s00603-016-1162-2

[61] Li, Y., Huang, D. and Li, X.A. (2014) Strain Rate Dependency of Coarse Crystal Marble under Uniaxial Compression: Strength, Deformation and Strain Energy. *Rock Mechanics and Rock Engineering*, **47**, 1153-1164. https://doi.org/10.1007/s00603-013-0472-x

[62] You, M. (2011) Strength and Damage of Marble in Ductile Failure. *Journal of Rock Mechanics and Geotechnical Engineering*, **3**, 161-166. https://doi.org/10.3724/SP.J.1235.2011.00161

[63] Wang, Y., Zhang, B., Gao, S.H. and Li, C.H. (2021) Investigation on the Effect of Freeze-Thaw on Fracture Mode Classification in Marble Subjected to Multi-Level Cyclic Loads. *Theoretical and Applied Fracture Mechanics*, **111**, Article ID: 102847. https://doi.org/10.1016/j.tafmec.2020.102847

[64] Wang, Y., Gao, S.H., Li, C.H. and Han, J.Q. (2021) Energy Dissipation and Damage Evolution for Dynamic Fracture of Marble Subjected to Freeze-Thaw and Multiple Level Compressive Fatigue Loading. *International Journal of Fatigue*, **142**, Article

ID: 105927. https://doi.org/10.1016/j.ijfatigue.2020.105927

[65] El Boudani, M., Wilkie-Chancellier, N., Martinez, L., Hébert, R., Rolland, O., Forst, S. and Serfaty, S. (2015) Marble Characterization by Ultrasonic Methods. *Procedia Earth and Planetary Science*, **15**, 249-256. https://doi.org/10.1016/j.proeps.2015.08.061

[66] Renard, F., Kandula, N., McBeck, J. and Cordonnier, B. (2020) Creep Burst Coincident with Faulting in Marble Observed in 4-D Synchrotron X-Ray Imaging Triaxial Compression Experiments. *Journal of Geophysical Research*: *Solid Earth*, **125**, e2020JB020354. https://doi.org/10.1029/2020JB020354

[67] De Bresser, J.H.P., Urai, J.L. and Olgaard, D.L. (2005) Effect of Water on the Strength and Microstructure of Carrara Marble Axially Compressed at High Temperature. *Journal of Structural Geology*, **27**, 265-281. https://doi.org/10.1016/j.jsg.2004.10.002

[68] Koch, A. and Siegesmund, S. (2004) The Combined Effect of Moisture and Temperature on the Anomalous Expansion Behaviour of Marble. *Environmental Geology*, **46**, 350-363. https://doi.org/10.1007/s00254-004-1037-9

[69] Ahmad, A. (2020) Investigation of Marble Deterioration and Development of a Classification System for Condition Assessment Using Non Destructive Ultra-Sonic Technique. *Mediterranean Archaeology and Archaeometry*, **20**, 75-89. https://doi.org/10.5281/zenodo.3930410

[70] Mahmutoğlu, Y. and Gökhan, Ş.A.N.S. (2020) Comparison of Post-Failure Strength of Micro-Cracked Marble with Hoek-Brown Failure Criterion. *Pamukkale Üniversitesi Mühendislik Bilimleri Dergisi*, **26**, 1365-1372. https://dergipark.org.tr/en/pub/pajes/issue/58157/838583

[71] Peng, J., Rong, G., Tang, Z. and Sha, S. (2019) Microscopic Characterization of Microcrack Development in Marble after Cyclic Treatment with High Temperature. *Bulletin of Engineering Geology and the Environment*, **78**, 5965-5976. https://doi.org/10.1007/s10064-019-01494-2

[72] Rong, G., Yao, M., Peng, J., Sha, S. and Tan, J. (2018) Influence of Initial Thermal Cracking on Physical and Mechanical Behaviour of a Coarse Marble: Insights from Uniaxial Compression Tests with Acoustic Emission Monitoring. *Geophysical Journal International*, **214**, 1886-1900. https://doi.org/10.1093/gji/ggy257

[73] Nara, Y., Kashiwaya, K., Nishida, Y. and Ii, T. (2017) Influence of Surrounding Environment on Subcritical Crack Growth in Marble. *Tectonophysics*, **706**, 116-128. https://doi.org/10.1016/j.tecto.2017.04.008

[74] Mahmutoğlu, Y. (2017) Prediction of Weathering by Thermal Degradation of a Coarse-Grained Marble Using Ultrasonic Pulse Velocity. *Environmental Earth Sciences*, **76**, 1-20. https://doi.org/10.1007/s12665-017-6770-y

[75] Liu, S. and Xu, J. (2015) Analysis on Damage Mechanical Characteristics of Marble Exposed to High Temperature. *International Journal of Damage Mechanics*, **24**, 1180-1193. https://doi.org/10.1177/1056789515570507

[76] Yao, M., Rong, G., Zhou, C. and Peng, J. (2016) Effects of Thermal Damage and Confining Pressure on the Mechanical Properties of Coarse Marble. *Rock Mechanics and Rock Engineering*, **49**, 2043-2054. https://doi.org/10.1007/s00603-016-0916-1

[77] Peng, J., Rong, G., Cai, M., Yao, M.D. and Zhou, C.B. (2016) Physical and Mechanical Behaviors of a Thermal-Damaged Coarse Marble under Uniaxial Compression. *Engineering Geology*, **200**, 88-93. https://doi.org/10.1016/j.enggeo.2015.12.011

[78] Rong, G., Peng, J., Yao, M., Jiang, Q. and Wong, L.N.Y. (2018) Effects of Specimen Size and Thermal-Damage on Physical and Mechanical Behavior of a Fine-Grained Marble. *Engineering Geology*, **232**, 46-55. https://doi.org/10.1016/j.enggeo.2017.11.011

[79] Liu, S. and Xu, J. (2013) Study on Dynamic Characteristics of Marble under Impact Loading and High Temperature. *International Journal of Rock Mechanics and Mining Sciences*, **62**, 51-58. https://doi.org/10.1016/j.ijrmms.2013.03.014

[80] Mahmutoğlu, Y. (2006) The Effects of Strain Rate and Saturation on a Micro-Cracked Marble. *Engineering Geology*, **82**, 137-144. https://doi.org/10.1016/j.enggeo.2005.09.001

[81] Ferrero, A.M. and Marini, P. (2001) Experimental Studies on the Mechanical Behaviour of Two Thermal Cracked Marbles. *Rock Mechanics and Rock Engineering*, **34**, 57-66. https://doi.org/10.1007/s006030170026

[82] Goudie, A.S. and Viles, H.A. (2010) Geomorphological Hazards and Disaster Prevention. Cambridge University Press, Cambridge, 145-160. https://doi.org/10.1017/CBO9780511807527.012

[83] Luque, A., Ruiz-Agudo, E., Cultrone, G., Sebastián, E. and Siegesmund, S. (2011) Direct Observation of Microcrack Development in Marble Caused by Thermal Weathering. *Environmental Earth Sciences*, **62**, 1375-1386. https://doi.org/10.1007/s12665-010-0624-1

[84] Siegesmund, S., Ullemeyer, K., Weiss, T. and Tschegg, E.K. (2000) Physical Weathering of Marbles Caused by Anisotropic Thermal Expansion. *International Journal of Earth Sciences*, **89**, 170-182. https://doi.org/10.1007/s005310050324

[85] Kadioğlu, S. and Kadioğlu, Y.K. (2006) Determination of Thicknesses and Discontinuities in a Marble Area by Ground Penetrating Radar (GPR) Method. *Journal of Engineering and Architectural Faculty of Selcuk University*, **21**, 127-136. https://dergipark.org.tr/tr/pub/sujest/issue/23271/248415

[86] Küçük, K. and Onargan, T. (2018) Evaluation of Block Efficiency in Burdur Beige Marble Quarry by Ground Penetrating Radar (GPR) Method. *Firat University Journal of Science*, **30**, 51-59. https://dergipark.org.tr/en/pub/fufbd/issue/35839/400753

[87] Kadıoğlu, S.P.Y. (2008) Determination of Discontinuities in the Purchase and Processing of Marble Blocks. Ankara University Press, Ankara. http://hdl.handle.net/20.500.12575/41388

[88] Pascale, G. and Lolli, A. (2015) Crack Assessment in Marble Sculptures Using Ultrasonic Measurements: Laboratory Tests and Application on the Statue of David by Michelangelo. *Journal of Cultural Heritage*, **16**, 813-821. https://doi.org/10.1016/j.culher.2015.02.005

[89] Ahmad, A. and Al-Bashaireh, K. (2021) Provenance Determination and Condition Assessment of Archaeological Marble Statues from Gerasa Using Non-Destructive Ultrasonic Technique. *Studies in Conservation*, **66**, 397-412. https://doi.org/10.1080/00393630.2020.1848268

[90] Menningen, J., Siegesmund, S., Tweeton, D. and Träupmann, M. (2018) Ultrasonic Tomography: Non-Destructive Evaluation of the Weathering State on a Marble Obelisk, Considering the Effects of Structural Properties. *Environmental Earth Sciences*, **77**, Article No. 601. https://doi.org/10.1007/s12665-018-7776-9

[91] Tiefensee, F., Weber, P., Kunz, S., Pamplona, M. and Simon, S. (2017) Ultrasonic Phased Array Technology for the Non-Destructive Testing of Marble Sculptures. *Studies in Conservation*, **62**, 55-60. https://doi.org/10.1080/00393630.2016.1141538

[92] Sassoni, E. and Franzoni, E. (2014) Sugaring Marble in the Monumental Cemetery in Bologna (Italy): Characterization of Naturally and Artificially Weathered Samples and First Results of Consolidation by Hydroxyapatite. *Applied Physics A*, **117**, 1893-1906. https://doi.org/10.1007/s00339-014-8629-3